

Article

# Frequency-Based Performance Analysis of an Array of Wave Energy Converters around a Hybrid Wind–Wave Monopile Support Structure

Sofia Gkaraklova, Pavlos Chotzoglou and Eva Loukogeorgaki \*

Department of Civil Engineering, Aristotle University of Thessaloniki, University Campus, 54124 Thessaloniki, Greece; sofentgka@civil.auth.gr (S.G.); pavchogeo@civil.auth.gr (P.C.)

\* Correspondence: eloukog@civil.auth.gr; Tel.: +30-2310-99-5951

**Abstract:** In this paper, we investigate, in the frequency domain, the performance (hydrodynamic behavior and power absorption) of a circular array of four semi-immersed heaving Wave Energy Converters (WECs) around a hybrid wind–wave monopile (circular cylinder). The diffraction/radiation problem is solved by deploying the conventional boundary integral equation method. Oblate-spheroidal and hemispherical-shaped WECs are considered. For each geometry, we assess the effect of the array’s net radial distance from the monopile and of the incident wave direction on the array’s performance under regular waves. The results illustrate that by placing the oblate spheroidal WECs close to the monopile, the array’s power absorption ability is enhanced in the low frequency range, while the opposite occurs for higher wave frequencies. For hemispherical-shaped WECs, the array’s power absorption ability is improved when the devices are situated close to the monopile. The action of oblique waves, with respect to the WECs’ arrangement, increases the absorbed power in the case of oblate spheroidal WECs, while these WECs show the best power absorption ability among the two examined geometries. Finally, for the most efficient array configuration, consisting of oblate spheroidal WECs situated close to the monopile, we utilize an “active” Power Take-Off (PTO) mechanism, facilitating the consideration of a variable with frequency PTO damping coefficient. By deploying this mechanism, the power absorption ability of the array is significantly enhanced under both regular and irregular waves.

**Keywords:** hybrid wind–wave system; wave energy converters; monopile; oblate spheroids; arrays; hydrodynamic analysis; power absorption; power take-off mechanism



**Citation:** Gkaraklova, S.; Chotzoglou, P.; Loukogeorgaki, E. Frequency-Based Performance Analysis of an Array of Wave Energy Converters around a Hybrid Wind–Wave Monopile Support Structure. *J. Mar. Sci. Eng.* **2021**, *9*, 2. <https://dx.doi.org/10.3390/jmse9010002>

Received: 15 November 2020

Accepted: 18 December 2020

Published: 22 December 2020

**Publisher’s Note:** MDPI stays neutral with regard to jurisdictional claims in published maps and institutional affiliations.



**Copyright:** © 2020 by the authors. Licensee MDPI, Basel, Switzerland. This article is an open access article distributed under the terms and conditions of the Creative Commons Attribution (CC BY) license (<https://creativecommons.org/licenses/by/4.0/>).

## 1. Introduction

The increase of energy demand, the rising cost of fossil fuels, and the environmental problems derived from their overexploitation have put a spotlight on renewable energy resources. Offshore renewable energy, which includes both the ocean (wave and tidal) energy and the mature, nowadays, offshore wind energy, has shown a great potential for development [1,2] and it is anticipated to play a fundamental role in the EU energy policy, as identified by the European Strategic Energy Technology Plan (SET-Plan). The set target for 2050 corresponds to 188 GW and 460 GW of installed capacity for ocean energy and offshore wind respectively [3,4]. As for the contribution of solely wave and offshore wind power to the EU electricity mix, the goal is to satisfy 15% of the European electricity demand and, in some countries, up to 20% of the national demand by 2050 [3].

Aiming at exploiting simultaneously both offshore wind and wave energy, Offshore Wind Turbines (OWTs) can be integrated with Wave Energy Converters (WECs). This integration can be realized in a twofold way by (a) locating OWTs and WECs in the same marine area, leading to the formation of the so-called “co-located parks” [4–7] and/or (b) combining offshore wind and wave energy technologies into one structure, resulting to the deployment of the so-called “hybrid systems” or “combined systems”. The latter systems

can be further categorized into bottom-mounted and floating ones, depending upon the type of the support structure utilized (bottom-mounted or floating platform, respectively). The advantages of combining offshore wind and wave energy technologies into a hybrid system are numerous (e.g., [4,5]). First of all, the energy yield per unit of marine surface is enhanced and, hence, better use of natural resources is achieved. Moreover, a smooth and more predictable power output can be realized, since the exploitation of the less variable and more predictable waves enables the avoidance of sudden losses in power generation due to unpredictable wind variations. One of the most considerable benefits is the decrease of the levelized cost of energy, as costs related to infrastructure, transmission, grid connection, permissions, and operation and maintenance are shared. Furthermore, the ecological footprint of a hybrid wind and wave energy exploitation system is expected to be smaller than that of the separate alternative [8,9]. However, there are a few challenges to overcome as well. The main problem is the different level of maturity of the two specific technologies. OWTs correspond to a well-established technology with a total installed capacity in Europe by the end of 2019 equal to 22.072 GW [10]. The wave energy industry, on the other hand, is still at a nascent phase. This is primarily due to the wide range of WECs' types available and the fact that most of them are still at early stages of development. The above items in combination with lack of practical experience and data related to combined technologies lead to an additional economic risk associated with hybrid projects [11].

Up until now there have been many investigations that focus on floating hybrid systems. Michailides et al. [12–14] proposed a semi-submersible flap type combined system (SFC system) and performed an integrated time domain numerical analysis of this system as well as relevant experiments. Muliawan et al. [15,16] conducted an integrated numerical and experimental analysis for the case of a spar-type floating wind turbine and a coaxial floating torus WEC (STC system). The performance of the aforementioned floating hybrid systems (SFC and STC) was also compared by Gao et al. [17] using both numerical and experimental data. Inspired by the STC system, a 5 MW wind turbine on a semi-submersible platform combined with a heaving WEC was investigated in [18]. The performance of a floating hybrid system with a Tension Leg Platform (TLP) and three point absorbers was numerically studied and assessed by [19], while in [20–22], the WindWEC system, combining a floating wind turbine on a spar and an oscillating in heave and pitch WEC buoy, was proposed and it was numerically investigated in time domain. A floating hybrid system consisting of a 5 MW wind turbine and oscillating water column devices moored using tensioned tethers in a TLP concept was investigated numerically and experimentally by [23]. Finally, Lee et al. [24] studied in the frequency domain the performance of multiple heaving WECs placed on a floating semi-submersible platform that can be utilized as a support structure of more than one wind turbines.

Contrary to the floating hybrid systems, the case of deploying a bottom-mounted hybrid system has been considered by a few researchers, who mainly focused on the design and the development of a WEC concept that can be utilized on a hybrid wind–wave bottom-mounted support structure. More specifically, Perez-Collazo et al. [25] carried out an experimental investigation of an oscillating water column WEC attached to hybrid wind–wave jacket support structure, while the aforementioned WEC type attached to a hybrid wind–wave monopile support structure has been the subject of the experimental research of [26]. Inspired by the STC floating hybrid system, a heaving WEC attached on hybrid wind–wave monopile support structure using a pulley slide mechanism was studied both numerically and experimentally in [27].

In the present paper, we numerically investigate the performance (hydrodynamic behavior and power absorption) of a circular array of four semi-immersed heaving WECs distributed uniformly around a hybrid wind–wave monopile support structure. The array consists of either hemispherical-shaped or oblate-spheroidal WECs, while each WEC is assumed to absorb power through a linear Power Take-Off (PTO) mechanism, actuated from its heave motion. The monopile corresponds to a bottom-mounted, surface-piercing circular cylinder. The examined WEC array and the monopile could be considered as

components of a new bottom-mounted hybrid offshore wind and wave energy exploitation system, which is proposed in this paper (Figure 1a). The system was inspired by Wave Treader [28] and Wave Star [29] and enables the motion of the WECs only along the vertical direction by attaching them on the monopile via arms, which move vertically along sliding guideways, i.e., sliders (Figure 1b). The analysis is implemented in the frequency domain under the action of regular, head, and oblique waves. The corresponding diffraction/radiation problem, taking into account the hydrodynamic interactions among the WECs and between the monopile and the WECs, is solved by utilizing the conventional Boundary Integral Equation (BIE) method. For each of the examined geometries and for a constant PTO damping coefficient, we initially present extended results in order to assess the effect of the net radial distance of the array from the monopile and of the incident wave direction on the hydrodynamic behavior and the power absorption ability of the array. Moreover, comparison with the case of an isolated array is performed in order to illustrate the effect of the existence of the monopile on the performance of the array. Finally, the most efficient array configuration (WECs' geometry and net radial distance) is chosen in order to further enhance its power absorption ability by appropriately adjusting the damping coefficient of the PTO mechanism along the examined frequency range (i.e., utilization of an "active" PTO mechanism). In this case, the power absorbed by the array is assessed for regular waves as well as for various sea states by utilizing the Jonswap spectrum.

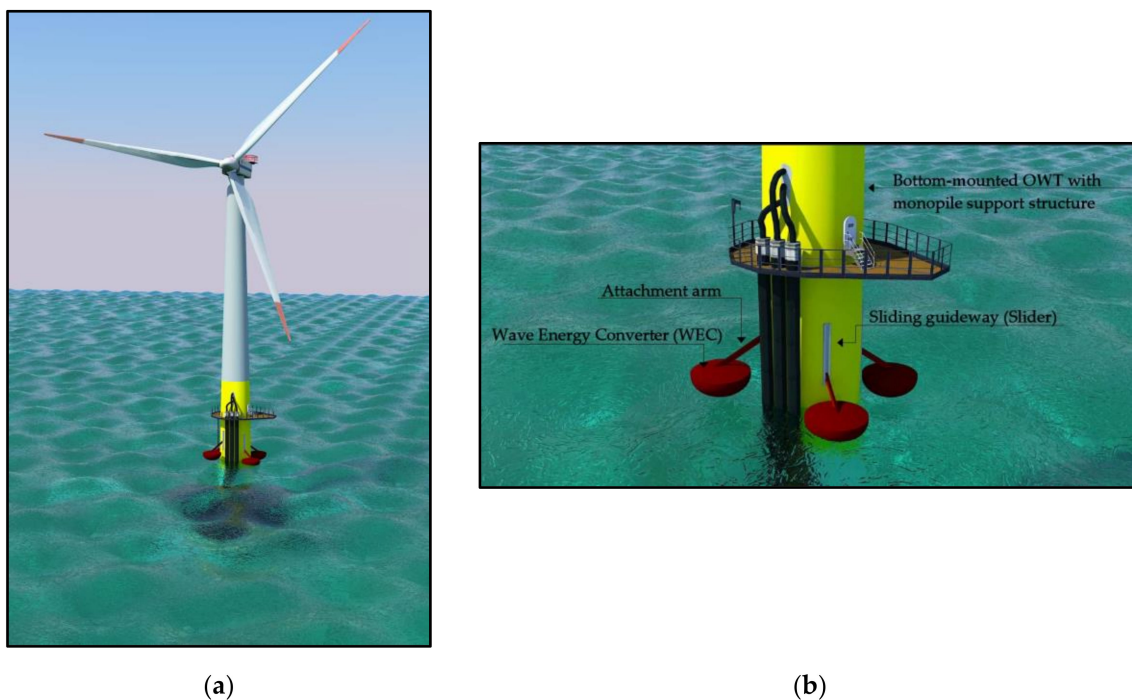


**Figure 1.** Proposed hybrid offshore wind and wave energy exploitation system: (a) conceptual representation; (b) view of the WECs' attachment on the bottom-mounted OWT.

## 2. Numerical Modeling

A circular array of  $M$  hydrodynamically interacting, semi-immersed heaving WECs is placed around a bottom-mounted cylindrical monopile in a marine region of constant water depth  $d$  (Figure 2). The array consists of identical WECs, which have either an oblate spheroidal shape or a hemispherical shape (with a short cylindrical upper part close to the waterline), as shown in Figure 3. The radius and the total draft of the WECs are denoted, respectively, as  $r_k$  and  $h_k$ , with  $k = 1$  corresponding to the dimensions of the oblate spheroidal WECs and  $k = 2$  to those of the hemispherical-shaped devices. Each heaving WEC is assumed to absorb power through a linear PTO mechanism, which is schematically

represented in Figure 2b as a linear damping system, with damping coefficient  $b_{PTOj}$ ,  $j = 1, \dots, M$ . All WECs are distributed uniformly in a circular arrangement around the monopile at a center-to-center radial distance equal to  $d_{radial}$  and net radial distance equal to  $d_{net}$  (Figure 2a). The monopile is modelled as a bottom-mounted, surface-piercing circular cylinder of radius  $r_0$  and of draft  $d$  (Figure 3). All bodies are subjected to the action of monochromatic incident waves of circular frequency  $\omega$  and linear amplitude  $A$ , which propagate at an angle  $\beta$  relative to the global horizontal  $X$ -axis (Figure 2a).

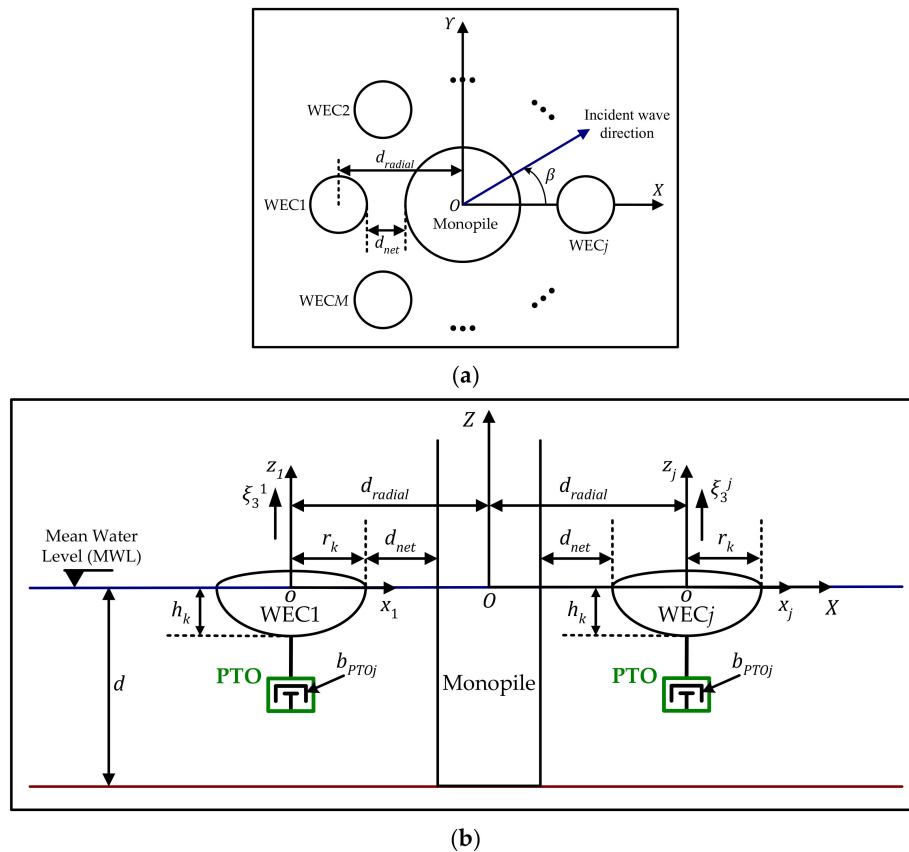


Figure 2. Geometry of the examined problem and definition of basic quantities: (a)  $X - Y$  plane; (b)  $X - Z$  plane.

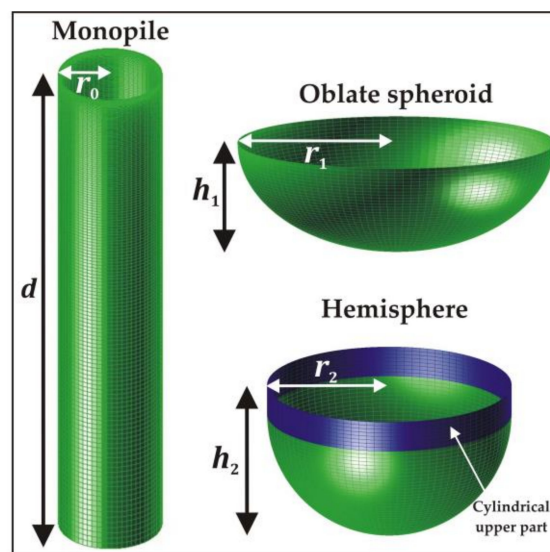


Figure 3. Submerged parts of all examined bodies.

The hydrodynamic analysis of the WEC circular array around the monopile, including the hydrodynamic interactions among all co-located bodies, is conducted in the frequency domain and it relies on the BIE method (e.g., [30–32]), which is numerically realized using WAMIT [33]. The analysis is based on a three-dimensional linear diffraction theory, where the monopile is considered to be fixed at its position, while all WECs are taken to undergo small amplitude oscillations only along the vertical  $z_j$ -axis, i.e., along their working direction (Figure 2b). Thus, for each WEC $j$ ,  $j = 1, \dots, M$ , all degrees of freedom, except the one corresponding to heave, are considered ideally restricted. Assuming inviscid and incompressible fluid with irrotational flow, the fluid motion is described by introducing the velocity potential. Its complex spatial part is defined as follows [33,34]:

$$\varphi = \underbrace{(\varphi_I + \varphi_S)}_{\varphi_D} + i\omega \sum_{j=1}^M \zeta_3^j \varphi_j \tag{1}$$

$$\varphi_I = \frac{igA}{\omega} \frac{\cosh[k(Z + d)]}{\cosh(kd)} e^{-ik(X\cos\beta + Y\sin\beta)} \tag{2}$$

where  $\varphi_I$  is the incident wave potential;  $\varphi_S$  is the scattered potential, related to the scattered disturbance of the incident waves from the WECs and the monopile;  $\varphi_D$  denotes the diffraction potential; and  $\varphi_j$ ,  $j = 1, \dots, M$ , correspond to the radiation potentials, associated with the waves radiated from the WECs due to their forced motion in heave, while  $\zeta_3^j$ ,  $j = 1, \dots, M$ , denote the complex amplitudes of the heave motions of the WECs. Furthermore,  $g$  is the gravitational acceleration,  $k$  is the wave number, and  $i^2 = -1$ .

The velocity potentials  $\varphi_q$  ( $q = D$  or  $q = j$ ) satisfy the Laplace equation everywhere in the fluid domain, while, additionally, they are subjected to the following linearized boundary conditions corresponding to the combined kinematic and dynamic free-surface condition (Equation (3)), the bottom boundary condition (Equation (4)), and the Neumann boundary conditions on the wetted surface of the bodies (Equations (5) and (6)) [33,34]:

$$\frac{\partial \varphi_q}{\partial Z} - \frac{\omega^2}{g} \varphi_q = 0 \text{ on } Z = 0 \tag{3}$$

$$\frac{\partial \varphi_q}{\partial Z} = 0 \text{ on } Z = -d \tag{4}$$

$$\frac{\partial \varphi_D}{\partial n} = 0 \tag{5}$$

$$\frac{\partial \varphi_j}{\partial n} = n_3^j \text{ for } j = 1, \dots, M \tag{6}$$

In Equation (6),  $n_3^j$  denotes the normal unit vector of WEC $j$  in the vertical direction.

Green’s theorem is employed to form the boundary integral equations for the unknown diffraction and radiation potentials on the boundaries of all bodies (WECs and monopile) and of the WECs, respectively. The corresponding first order boundary value problem is then solved on the basis of the three dimensional low-order panel method [33,34].

Having solved the aforementioned boundary value problem, we calculate the first-order hydrodynamic forcing quantities as follows:

$$F_l = -i\omega\rho \iint_{S_b^m} n_l \varphi_D ds, \quad l = 1, 2 \tag{7}$$

$$F_3^i = -i\omega\rho \iint_{S_b^i} n_3^i \varphi_D ds, \quad i = 1, \dots, M \tag{8}$$

$$A_{ij} - \frac{i}{\omega} B_{ij} = \rho \iint_{S_b^i} n_3^i \varphi_j ds, \quad i, j = 1, \dots, M \tag{9}$$

where  $F_l$ ,  $l = 1, 2$ , is the surge and the sway exciting force respectively applied on the monopile;  $F_3^i$ ,  $i = 1, \dots, M$ , is the heave exciting force applied on each WEC;  $A_{ij}$  and  $B_{ij}$  correspond to the added mass and radiation damping coefficients, respectively;  $S_b^m$  is the wetted surface of the monopile;  $n_l$ ,  $l = 1, 2$ , denote the normal unit vector on  $S_b^m$  in the  $x$  and  $y$  directions, respectively;  $S_b^i$  is the wetted surface of the  $i^{\text{th}}$  WEC; and  $\rho$  is the water density.

The complex amplitudes of the WECs' heave motions,  $\zeta_3^j$ ,  $j = 1, \dots, M$ , are, then, obtained by solving the following linear system of equations:

$$\sum_{j=1}^M \left[ -\omega^2 (M_{ij} + A_{ij}) + i\omega (B_{ij} + B_{ij}^{PTO}) + C_{ij} \right] \zeta_3^j = F_3^i \quad i = 1, \dots, M \quad (10)$$

where  $M_{ij}$  are the mass matrix coefficients;  $C_{ij}$  are the hydrostatic-gravitational stiffness coefficients;  $A_{ij}$  and  $B_{ij}$  are the added mass and the radiation damping coefficients, respectively, as defined in Equation (9); and  $B_{ij}^{PTO}$  correspond to the damping coefficients originating from the PTO mechanism. For a  $j^{\text{th}}$  WEC of the array, this mechanism is modeled as a linear damping system (Figure 2b), which is actuated by the heave motion of the corresponding WEC and it has a damping coefficient  $b_{PTOj}$ . Thus, in Equation (10),  $B_{ij}^{PTO} = b_{PTOj}$  for  $i = j = 1, \dots, M$ , while  $B_{ij}^{PTO} = 0$  for  $i \neq j$ .

The heave response of each WEC is expressed in terms of the response amplitude operator as

$$RAO_3^j = \frac{|\zeta_3^j|}{A} \quad (11)$$

where  $|\zeta_3^j|$  denotes the amplitude of the complex quantity  $\zeta_3^j$ .

The mean power,  $p(\omega)$ , absorbed by the whole array of the WECs at a given  $\omega$  is obtained as

$$p(\omega) = \sum_{j=1}^M p_j(\omega) \quad (12)$$

where  $p_j(\omega)$ ,  $j = 1, \dots, M$ , correspond to the power absorbed by the  $j^{\text{th}}$  WEC, calculated using the following equation:

$$p_j(\omega) = 0.5 b_{PTOj} \omega^2 |\zeta_3^j|^2 \quad (13)$$

### 3. Characteristics of the Physical Problem Examined

The BIE-based numerical model described in Section 2 is applied for the case of a monopile of radius  $r_0 = 4.0$  m and an array of  $M = 4$  identical, semi-immersed WECs with the layout shown in Figure 4. All bodies are placed in an area of constant water depth  $d = 40.0$  m. The oblate spheroidal WECs (Figure 3) have radius  $r_1 = 2.5$  m and total draft  $h_1 = 1.7$  m. The corresponding dimensions of the hemispherical-shaped WECs (Figure 3) are defined as equal to  $r_2 = 2.0$  m and  $h_2 = 2.5$  m (0.5 m correspond to the cylindrical upper part), aiming at comparing different shaped WECs that have similar submerged volumes,  $V$ , as well as similar heave natural frequencies,  $\omega_{n3}^{ISO}$  (Table 1). For a given geometry, all WECs within the array are considered to have the same PTO characteristics; thus, in Equation (10),  $B_{ij}^{PTO} = b_{PTO}$  for  $i = j = 1, \dots, 4$ . Furthermore, the constant PTO damping coefficient,  $b_{PTO}$ , is appropriately tuned in terms of maximizing energy absorption at the natural frequency of the corresponding single, isolated WEC. On the basis of this and along the lines of [35],  $b_{PTO}$  is taken to be equal to the heave radiation damping coefficient of a single, isolated oblate spheroidal or hemispherical-shaped WEC at its heave natural frequency,  $\omega_{n3}^{ISO}$ , namely,  $b_{PTO} = B_{33}^{ISO}(\omega = \omega_{n3}^{ISO})$ . The values of  $\omega_{n3}^{ISO}$  and  $b_{PTO}$  for both examined geometries obtained by the hydrodynamic analysis of the corresponding single, isolated body are presented in Table 1. It is evident that the existence

of different hydrodynamic properties among the examined geometries lead to different  $b_{PTO}$  values.

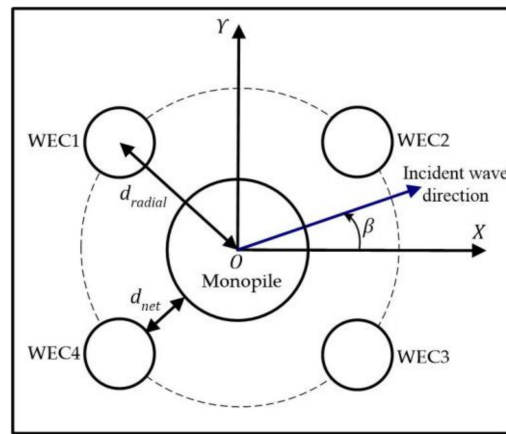


Figure 4. Examined layout of the array with  $M = 4$  WECs.

Table 1. Geometrical and hydrodynamic properties of WEC geometries examined.

Geometry	$r_k$ (m)	$h_k$ (m)	$V$	$C_{33}$ (kN/m)	$\omega_{n3}^{ISO}$ (rad/s)	$b_{PTO}$ (kNs/m)
Oblate spheroid	2.5	1.7	22.150	197.076	2.282	20.615
Hemisphere	2.0	2.5 <sup>1</sup>	22.935	125.969	2.008	6.673

<sup>1</sup> 0.5 m correspond to the cylindrical upper part.

For each WEC geometry, we, initially examine and assess the effect of the net radial distance of the array from the monopile,  $d_{net}$ , and of the incident wave direction,  $\beta$  (Figure 4) on the performance of the array under the action of regular waves, with  $\omega$  varying between 0.02 and 4.5 rad/s. Regarding the net radial distance, seven different values of  $d_{net}$  are examined (Table 2) for head incident waves (i.e.,  $\beta = 0^\circ$ , Figure 4), while furthermore, representative results are compared with those of isolated arrays (i.e., without the monopile), aiming at illustrating more clearly the effect of the presence of the monopile on the power absorption ability of the WECs. With regard to the incident wave direction, we take three different values of  $\beta$ , representing head and oblique waves, into account (Table 2) for  $d_{net} = 0.125r_0$  (oblate spheroidal WECs) and  $d_{net} = 0.25r_0$  (hemispherical-shaped WECs). Finally, the most efficient array configuration (WECs' geometry and net radial distance) is chosen in order to further enhance its power absorption ability by adjusting appropriately the damping coefficient of the linear PTO mechanism along the examined frequency range (i.e., utilization of an “active” PTO mechanism). In this case, the power absorbed by the array is assessed for both regular and irregular waves with  $\beta = 45^\circ$ . More details about this “active” PTO mechanism are cited in Section 4.4, where the corresponding results are presented.

Table 2. Examined cases for the array with  $M = 4$  WECs.

Design Parameter	WEC Geometry	$d_{net}$ (m)	$\beta$ (°)
Net radial distance ( $d_{net}$ )	Oblate spheroid, Hemisphere	$0.125r_0, 0.25r_0, 0.5r_0, 0.75r_0, 1.0r_0, 1.25r_0, 1.5r_0$	0
Incident wave direction ( $\beta$ )	Oblate spheroid, Hemisphere	$0.125r_0, 0.25r_0$	0, 22.5, 45

#### 4. Results and Discussion

##### 4.1. Effect of Net Radial Distance on the Performance of the Array with Oblate Spheroidal WECs

The effect of the net radial distance of the oblate spheroidal WECs from the monopile on the WECs' non-dimensional (in terms of  $\rho g A \pi r_1^2$ ) heave exciting forces is shown in Figure 5, where the variation of  $F_3$  for all WECs of the circular array is presented as a function of  $\omega$  for all examined  $d_{net}$  values. The symmetry of the array with respect to  $\beta = 0^\circ$  (Figure 4) leads to the same values of  $F_3$  for the WECs situated in the seaward side of the monopile (i.e., WEC1 and WEC4, Figure 4) as well as for those situated in the leeward side of the bottom-mounted support structure (i.e., WEC2 and WEC3, Figure 4).

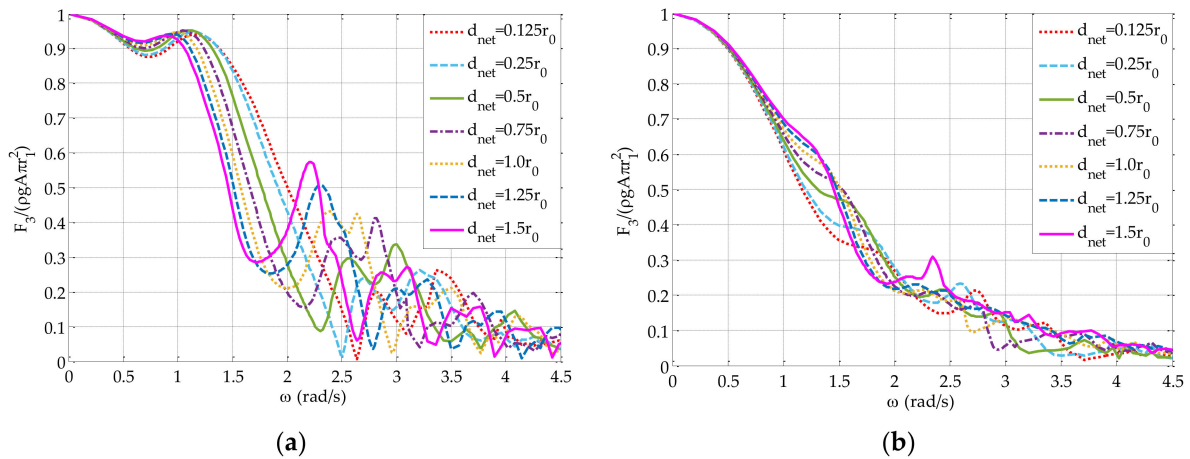


**Figure 5.** Effect of  $d_{net}$  on the non-dimensional heave exciting forces applied on the oblate spheroidal WECs placed around the monopile for  $\beta = 0^\circ$  : (a) WEC1 and WEC4; (b) WEC2 and WEC3.

Considering the WECs placed in the seaward side of the monopile (Figure 5a), the variation of the non-dimensional heave exciting force for the smallest examined net radial distance,  $d_{net} = 0.125r_0$ , starts from the limiting value of  $\approx 1.00$  at  $\omega = 0.02$  rad/s and it is characterized by an almost smooth plateau up to  $\omega \approx 1.2$  rad/s, followed by a rapid decrease up to  $\omega \approx 2.6$  rad/s, where  $F_3$  obtains its first local minimum with a value almost equal to zero. Then,  $F_3$  varies quite intensively and obtains two local maxima at  $\omega \approx 2.8$  rad/s and  $\omega \approx 3.3$  rad/s. A similar variation pattern is observed for the rest of the  $d_{net}$  values examined. However, by successively increasing the WECs' net radial distance from the monopile, the extent of the aforementioned plateau is gradually reduced, while the first local minimum obtains non-zero values and it is shifted at lower frequencies. This, in turn, leads to larger values of the first  $F_3$  local peak, which, moreover, occur at lower wave frequencies. Overall, it can be stated that the placement of the array close to the monopile (i.e., at  $d_{net} \leq 0.5r_0$ ) leads to significant values of  $F_3$  at  $0.02$  rad/s  $< \omega < 1.4$  rad/s; however, at the same time, it results in a substantial decrease of  $F_3$  at  $2.0$  rad/s  $< \omega < 2.5$  rad/s, where resonance phenomena of the oblate spheroidal WECs are anticipated. The latter feature is not observed for  $d_{net} \geq 0.75r_0$ , where the relevant diffracted disturbances induced by the WECs and the monopile, as physically interpreted in the following paragraph, enable the formation of  $F_3$  peaks at  $2.0$  rad/s  $< \omega < 2.5$  rad/s. Regarding WEC2 and WEC3 (Figure 5b), their placement in the leeward side of the monopile, where shadow effects are induced by both the monopile and the seaward WECs, results in a smoother variation of the heave exciting forces compared to those applied on WEC1 and WEC4, while, moreover, the change of  $d_{net}$  has a small effect on the values and the variation pattern of  $F_3$ .

Coming back to the characteristic  $F_3$  local minima observed in the case of the seaward WECs (Figure 5a), their occurrence is attributed to the hydrodynamic interactions among the WECs as well as between the WECs and the monopile. For physically interpreting this, we take into account the spatial variation of the non-dimensional wave elevation,  $\eta_D/A$ , due to diffracted waves only. More specifically, Figure 6 shows the  $\eta_D/A$  spatial

variation indicatively for  $d_{net} = 0.125r_0$  and  $1.0r_0$  calculated at  $-16\text{ m} \leq X \leq 16\text{ m}$  and  $-16\text{ m} \leq Y \leq 16\text{ m}$  and for  $\omega \approx 2.6\text{ rad/s}$ . At this frequency,  $F_3$  of WEC1 and WEC4 obtains a characteristic local minimum for  $d_{net} = 0.125r_0$ , while the opposite holds true for  $d_{net} = 1.0r_0$  (Figure 5a). In the case of the smallest examined  $d_{net}$  value (Figure 6a), the variation pattern of  $\eta_D/A$  in the seaward side of the monopile (i.e., at  $X > 0\text{ m}$ ) is quite smooth and is characterized by the existence of well-formed lengthwise zones along the  $Y$ -axis, where  $\eta_D/A$  has values almost equal to zero. The positioning of WEC1 and WEC4 within one of these zones leads in turn to the existence of an almost symmetric, with respect to these WECs' local horizontal axes, diffracted wave field around them, with quite small  $\eta_D/A$  values. On the other hand, by placing WEC1 and WEC4 further from the monopile (Figure 6b), the diffraction disturbances induced by WEC1, WEC4, and the monopile are amplified in the seaward side of the monopile. As a result, a non-symmetric diffracted wave field with significant  $\eta_D/A$  values is formed around WEC1 and WEC4. All of the above advocate the existence of a very small  $F_3$  value for  $d_{net} = 0.125r_0$  at  $\omega \approx 2.6\text{ rad/s}$  contrary to  $d_{net} = 1.0r_0$ , in absolute accordance with the results of Figure 5a.

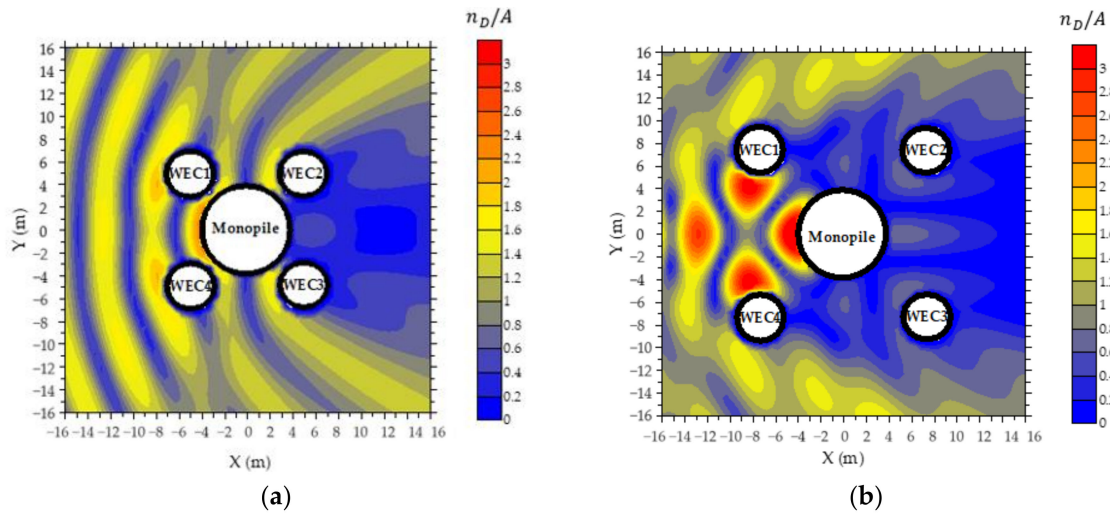


**Figure 6.** Spatial variation of the non-dimensional wave elevation,  $n_D/A$ , around the monopile and the oblate spheroidal WECs at  $\omega \approx 2.6\text{ rad/s}$  and for  $\beta = 0^\circ$ : (a)  $d_{net} = 0.125r_0$ ; (b)  $d_{net} = 1.0r_0$ .

Continuing with the response of the oblate spheroidal WECs, Figure 7 shows the effect of  $d_{net}$  on  $RAO_3$ . In the case of WEC1 and WEC4 (Figure 7a),  $RAO_3$  for all  $d_{net}$  values examined obtains a global peak at  $1.0\text{ rad/s} < \omega < 1.5\text{ rad/s}$  in absolute accordance with the variation of the corresponding heave exciting forces (Figure 5a). The largest peak value occurs for  $d_{net} = 0.125r_0$ , while by gradually increasing  $d_{net}$ , the peak values are successively decreased, following the relevant trend of  $F_3$  (Figure 5a). For the four largest examined  $d_{net}$  values, a second  $RAO_3$  peak occurs at  $2.0\text{ rad/s} < \omega < 2.5\text{ rad/s}$  due to resonance phenomena. However, this is not observed for  $d_{net} \leq 0.5r_0$ , due to the rapid decrease of  $F_3$  in this frequency range (Figure 5a) for the reasons previously explained. For  $\omega > 2.5\text{ rad/s}$ ,  $RAO_3$  for all  $d_{net}$  values shows an intense variation with successively decreasing values towards higher frequencies. As for the WECs situated in the leeward side of the monopile (Figure 7b), the change of  $d_{net}$  has a small effect on the values and the variation pattern of  $RAO_3$ , while for all  $d_{net}$  values investigated,  $RAO_3$  varies quite smoothly. These trends are in absolute accordance with those observed for the case of the corresponding heave exciting forces (Figure 5b).

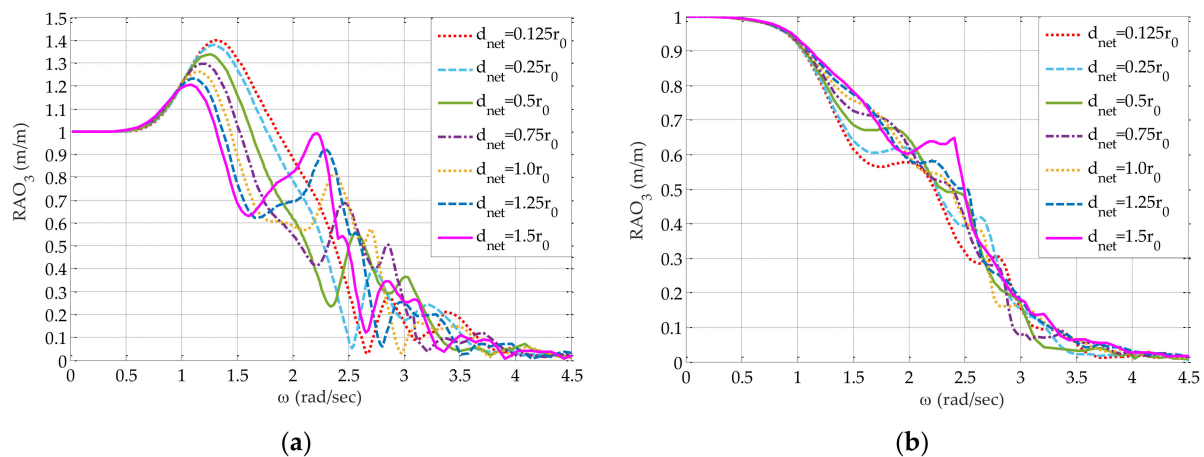


**Figure 7.** Effect of  $d_{net}$  on the heave response of the oblate spheroidal WECs placed around the monopile for  $\beta = 0^\circ$  : (a) WEC1 and WEC4; (b) WEC2 and WEC3.

Figure 8 shows the effect of  $d_{net}$  on the mean power absorbed by each oblate spheroidal WEC,  $p_j(\omega)$  (Figure 8a,b), as well as on the mean power absorbed by the whole array,  $p(\omega)$  (Figure 8c). When observing Figure 8a,b, one can easily realize the direct dependence of  $p_j(\omega)$ ,  $j = 1, \dots, 4$ , upon the heave responses (Figure 7), since for a given  $j$ th WEC, the variation patterns of  $p_j$  and  $RAO_3^j$  are very similar. Regarding WEC1 and WEC4, situated in the seaward side of the monopile (Figure 8a), it is evident that up to  $\omega = 2.0$  rad/s, these WECs show better absorption ability for small net radial distances from the monopile (i.e.,  $d_{net} \leq 0.5r_0$ ), whereas at higher frequencies (i.e.,  $2.0$  rad/s  $< \omega < 2.5$  rad/s), WEC1 and WEC4 are more efficient for  $d_{net}$  values larger than  $0.5r_0$ . From a physical point of view, the above conclusions can be explained as follows. For  $d_{net} \leq 0.5r_0$ , the power absorption ability of the seaward WECs is not driven by resonance phenomena, as large heave exciting forces and significant responses exist at wave frequencies outside the range where WECs' resonance occurs. However, the opposite holds true for  $d_{net} \geq 0.75r_0$ , where the hydrodynamic interactions among the WECs and between the WECs and the monopile do not impose any restrictions on the  $RAO_3$  amplification of the seaward WECs due to resonance. The WECs placed in the leeward side of the monopile (Figure 8b) are not strongly affected by the change of  $d_{net}$ . However, for  $d_{net} = 1.5r_0$ , they demonstrate a better power absorption ability at  $2.0$  rad/s  $< \omega < 2.5$  rad/s, in absolute accordance with the variation of the corresponding heave response (Figure 7b). Moreover, WEC2 and WEC3 show a reduced energy absorption ability compared to WEC1 and WEC4; hence, the variation pattern of the mean power absorbed by the whole array, as shown in Figure 8c, is significantly affected by the features of the power absorption curves related to the WECs situated in the seaward side of the monopile. Consequently, regarding the effect of  $d_{net}$  on the power absorption ability of the whole array, similar conclusions to those derived for WEC1 and WEC4 hold true.

Having this in mind, the results of Figure 8c illustrate that the placement of the WECs at  $d_{net} = 0.125r_0$  leads to an array that shows the best power absorption ability in the low examined frequency range among all examined  $d_{net}$  cases, with a  $p(\omega)$  peak value approximately equal to  $100$  kW/m<sup>2</sup>. Moreover, for this net radial distance, the frequency range where adequate amount of power is absorbed is quite wide. These features can be physically interpreted by using a similar rationale as in the case WEC1 and WEC4 for  $d_{net} \leq 0.5r_0$ . On the other hand, at higher wave frequencies, the array placed at  $d_{net} = 1.5r_0$  from the monopile shows the best power ability among all examined  $d_{net}$  cases, having a sharp  $p(\omega)$  peak with a value approximately equal to  $150$  kW/m<sup>2</sup>. Although the latter value is larger compared to the corresponding one of  $100$  kW/m<sup>2</sup> obtained for  $d_{net} = 0.125r_0$ , the placement of the WECs at  $d_{net} = 1.5r_0$  results in a more narrower frequency range, where adequate amount of power is absorbed. This is attributed to the

fact that for  $d_{net} = 1.5r_0$ , the power absorption ability of the seaward WECs and, thus, of the whole array is mainly driven by resonance phenomena. Taking all the above into account,  $d_{net} = 0.125r_0$  is chosen as the most appropriate net radial distance for placing the oblate spheroidal WECs around the monopile and it is considered for further investigation. This choice is also supported by the fact that most marine areas, including those in the North Sea, where the proposed hybrid offshore wind and wave energy exploitation system could be deployed, are mainly characterized by low-frequency sea waves (e.g., [36]).

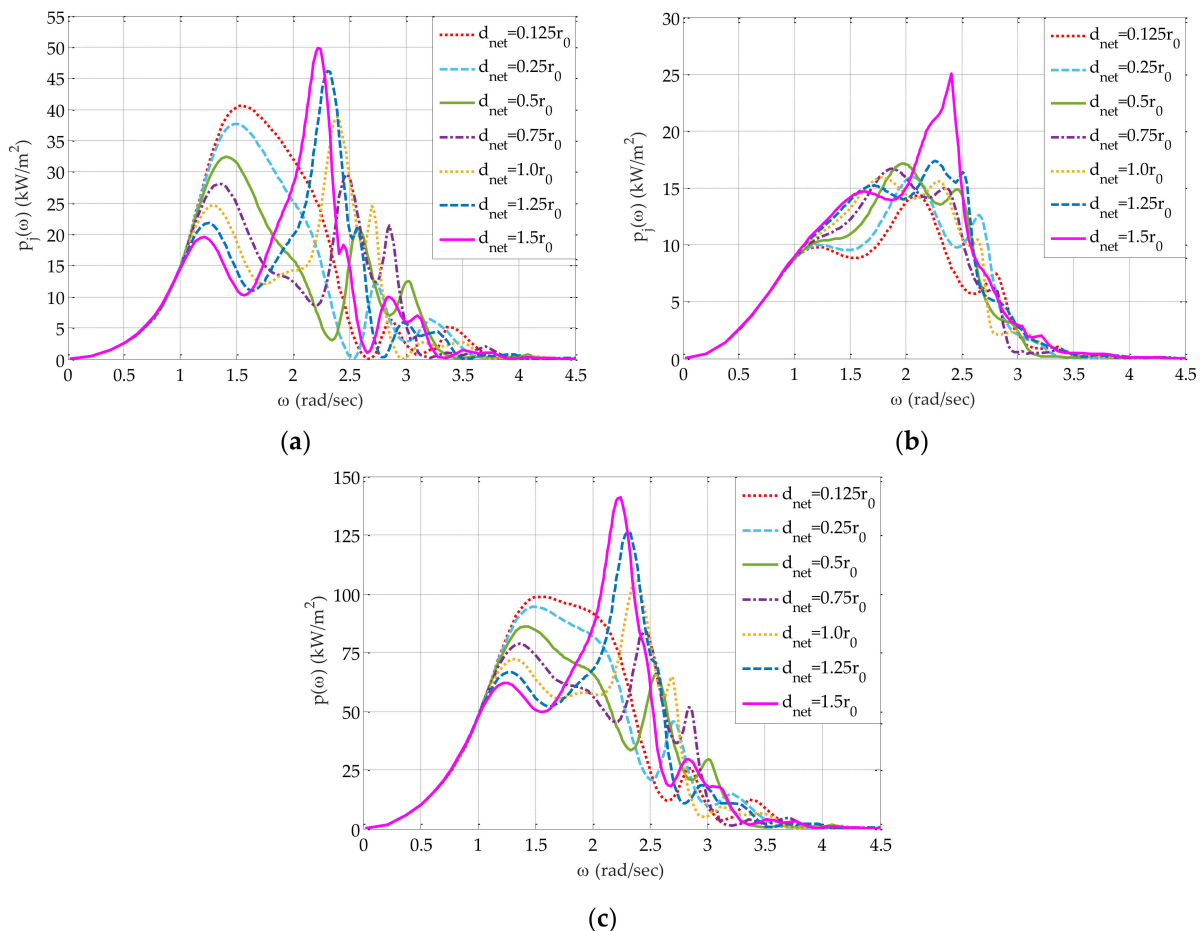


**Figure 8.** Effect of  $d_{net}$  on the mean power absorbed by the oblate spheroidal WECs placed around the monopile for  $\beta = 0^\circ$ : (a) WEC1 and WEC4; (b) WEC2 and WEC3; (c) whole array.

In order to illustrate more clearly the effect of the presence of the monopile on the power absorption ability of the oblate spheroidal WECs, we made a comparison of  $p_j(\omega)$ ,  $j = 1, \dots, 4$ , and  $p(\omega)$  for  $d_{net} = 0.125r_0$  with and without (i.e., isolated array) the monopile. The corresponding results are shown in Figure 9. For WEC1 and WEC4 situated in the seaward side of the monopile (Figure 9a), the existence of the latter structure positively affects their power absorption ability, since it leads to an  $\approx 15\%$  increase of the  $p_j(\omega)$ ,  $j = 1$  and 4, peak value, as well as to a much wider frequency range where adequate amount of power is absorbed. This is attributed to the existence of larger heave exciting forces of WEC1 and WEC4 at  $1.0 \text{ rad/s} < \omega < 2.0 \text{ rad/s}$ , due to the diffraction disturbances induced by the monopile, that, in turn, lead to larger heave responses of these WECs (relevant results are not included here due to space constraints). However, the shadow effects induced by the bottom-mounted cylinder reduce the power absorption ability of the WECs situated in the leeward side of the monopile (Figure 9b) at almost the whole examined frequency range. This in turn reduces at a small percentage ( $\approx 8\%$ ) the peak value of the power absorbed by the whole array compared to the isolated one (Figure 9c).

Nevertheless, the presence of the monopile enhances the power absorption ability of the whole array at a quite wide frequency range (i.e.,  $1.0 \text{ rad/s} < \omega < 1.9 \text{ rad/s}$ ).

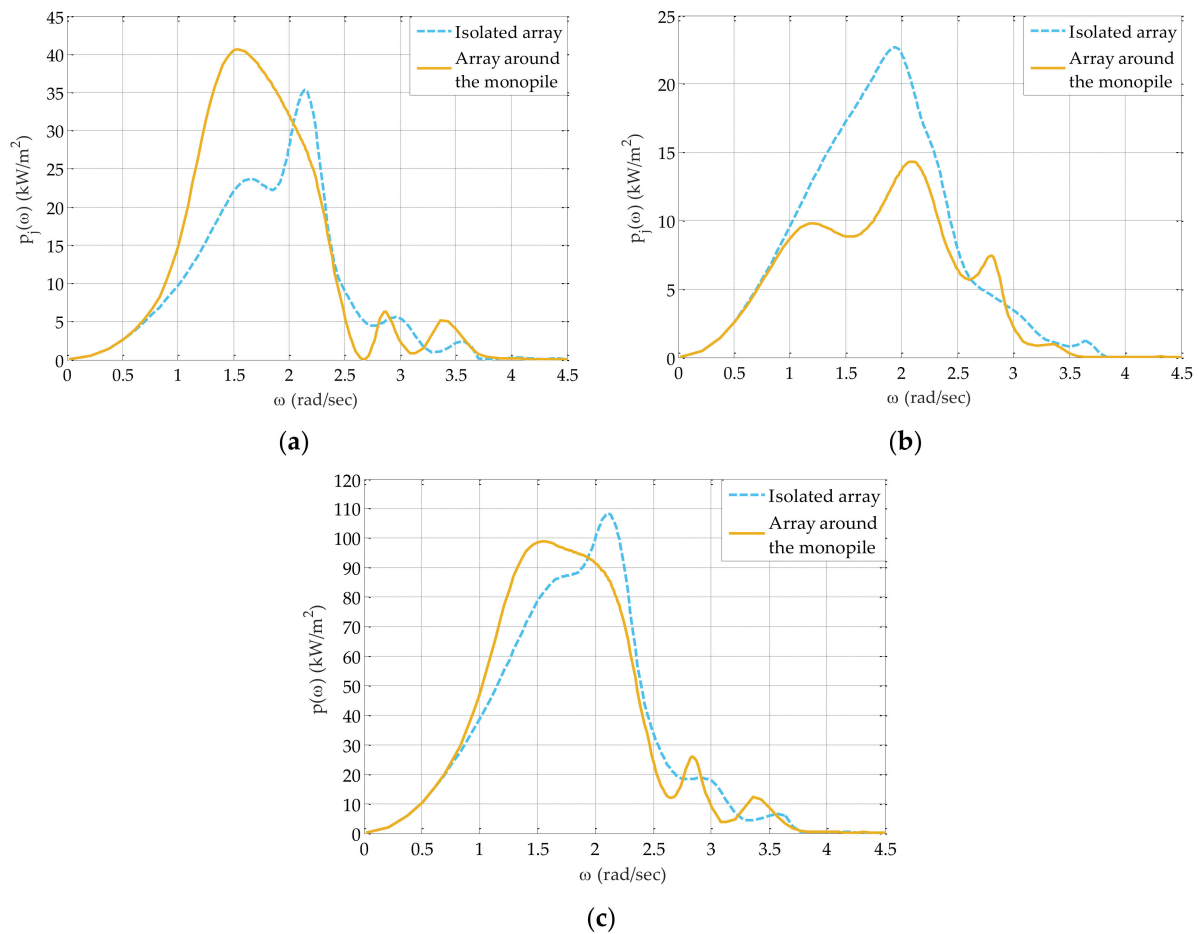


**Figure 9.** Comparison of the mean power absorbed by the oblate spheroidal WECs with and without (isolated array) the monopile for  $\beta = 0^\circ$  and  $d_{net} = 0.125r_0$ : (a) WEC1 and WEC4; (b) WEC2 and WEC3; (c) whole array.

Finally, it is interesting to demonstrate the effect of the presence of the oblate spheroidal WECs on the hydrodynamic loading applied on the monopile. This is realized with the aim of Figure 10, where the non-dimensional (in terms of  $\rho g A r_0^2$ ) surge exciting forces applied on the monopile for all  $d_{net}$  values examined are compared with those applied on the isolated (i.e., without the WEC array) monopile. It is evident that the presence of the WECs, irrespective of their net radial distance from the monopile, affects the surge exciting force of the bottom-mounted cylinder at  $\omega > 2.0 \text{ rad/s}$ , since in this frequency range,  $F_1$  does not demonstrate a continuous smooth decrease as in the case of the isolated monopile. From a physical point of view, this can be related to the diffraction disturbances induced by the WECs, which are anticipated to be more pronounced at higher frequencies (i.e., for shorter wave lengths) due to WECs’ geometrical characteristics.

#### 4.2. Effect of Net Radial Distance on the Performance of the Array with Hemispherical-Shaped WECs

For the array consisting of hemispherical-shaped WECs, we focus on the effect of the net radial distance of the WECs from the monopile on the WECs’ heave responses (Figure 11) and on the power absorbed by them (Figure 12). With regard to the heave exciting forces, similar conclusions can be drawn as in the case of the oblate spheroidal WECs and, thus, relevant results are not included due to space constraints.

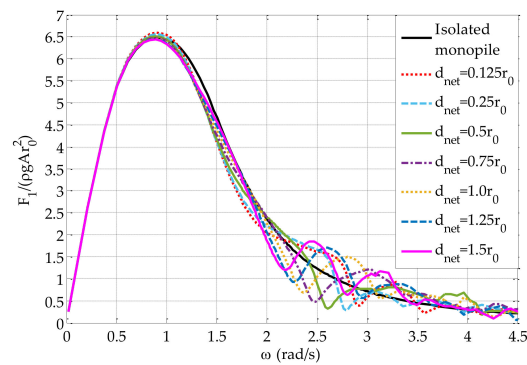


**Figure 10.** Comparison of the non-dimensional surge exciting forces applied on the monopile with and without (isolated monopile) the oblate spheroidal WECs for  $\beta = 0^\circ$ .

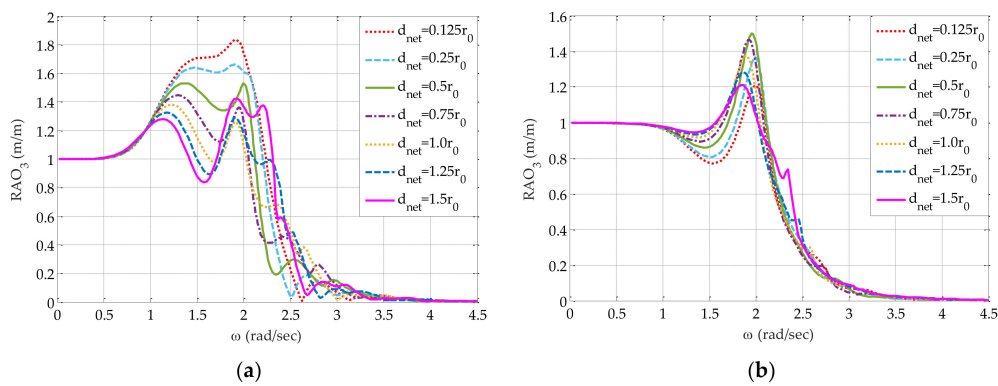


**Figure 11.** Effect of  $d_{net}$  on the heave response of the hemispherical-shaped WECs placed around the monopile for  $\beta = 0^\circ$ : (a) WEC1 and WEC4; (b) WEC2 and WEC3.

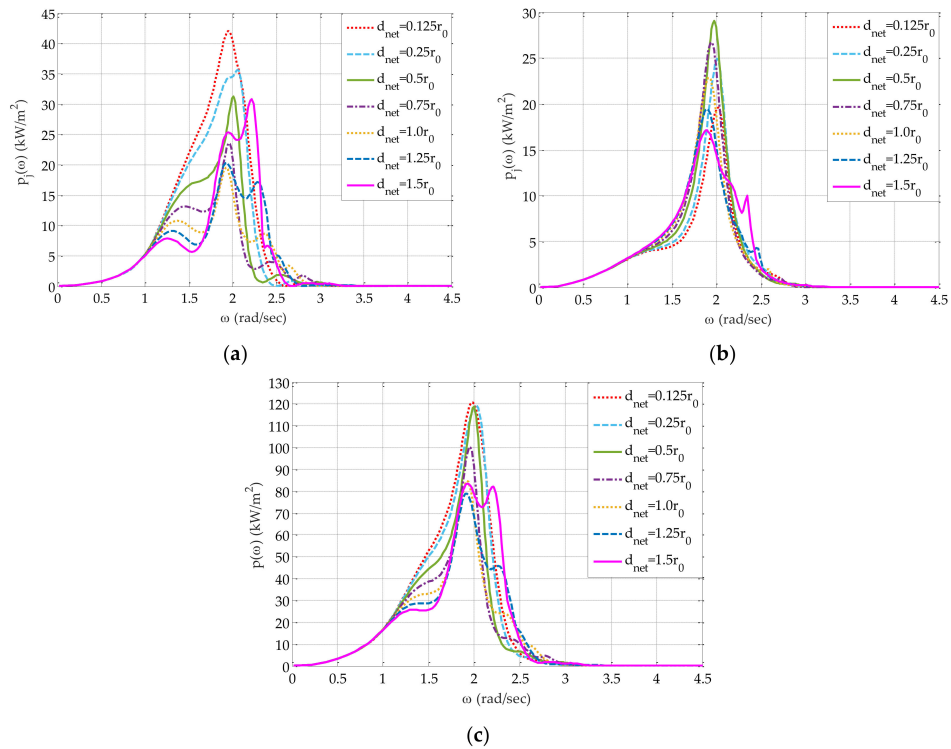


**Figure 12.** Effect of  $d_{net}$  on the mean power absorbed by the hemispherical-shaped WECs placed around the monopile for  $\beta = 0^\circ$ : (a) WEC1 and WEC4; (b) WEC2 and WEC3; (c) whole array.

With regard to the effect of  $d_{net}$  on the WECs' heave responses (Figure 11),  $RAO_3$  of WEC1 and WEC4 situated in the seaward side of the monopile (Figure 11a) obtains a peak at  $1.7 \text{ rad/s} < \omega < 2.3 \text{ rad/s}$  due to resonance phenomena for all  $d_{net}$  values examined. The largest peak value is observed for  $d_{net} = 0.125r_0$ , while the gradual increase of  $d_{net}$  leads successively to smaller  $RAO_3$  peak values. For the arrays with  $d_{net} \geq 0.5r_0$ , a characteristic local minimum also occurs at  $1.3 \text{ rad/s} < \omega < 1.9 \text{ rad/s}$  in absolute accordance with the variation of the corresponding heave exciting forces. Finally, for  $\omega > 2.3 \text{ rad/s}$ ,  $RAO_3$  for all  $d_{net}$  values shows an intense variation with continuously decreasing values towards higher frequencies. As for WEC2 and WEC3 situated in the leeward side of the monopile (Figure 11b), the change of  $d_{net}$  has a small effect on the values and the variation pattern of  $RAO_3$ . Compared to the oblate spheroidal WECs (Figure 7), the utilization of hemispherical-shaped WECs leads to larger  $RAO_3$  peak values related to resonance phenomena. This is mainly attributed to the consideration of a smaller  $b_{PTO}$  value for the hemispherical-shaped WECs (Table 1), as a result of their intrinsic hydrodynamic characteristics (i.e., existence of smaller heave radiation damping coefficients).

As for the power absorption ability of the hemispherical-shaped WECs, Figure 12 shows the effect of  $d_{net}$  on the mean power absorbed by each WEC,  $p_j(\omega)$  (Figure 12a,b), as well as on the mean power absorbed by the whole array,  $p(\omega)$  (Figure 12c). In general, the variation of  $p_j(\omega)$ ,  $j = 1, \dots, 4$ , follows the variation pattern of the corresponding  $RAO_3^j$  (Figure 11). In the case of WEC1 and WEC4 (Figure 12a), it is evident that the placement of these WECs at the smallest examined net radial distance from the monopile (i.e.,  $d_{net} = 0.125r_0$ ) leads to the largest  $p_j(\omega)$  peak, with a value approximately equal to  $40 \text{ kW/m}^2$ . By increasing  $d_{net}$  up to  $1.0r_0$ , a gradual decrease of the  $p_j(\omega)$  peak values occurs, while the opposite trend is observed for the largest examined  $d_{net}$  values. Moreover, for  $d_{net} > 0.5r_0$ , an intense decrease of  $p_j(\omega)$  occurs at  $1.1 \text{ rad/s} < \omega < 1.8 \text{ rad/s}$ . For the WECs situated in the leeward side of the monopile (Figure 12b) and contrary to WEC1 and WEC4, the increase of  $d_{net}$  up to  $0.5r_0$  results successively in larger power peak values, while the opposite trend occurs for the rest examined  $d_{net}$  values. Hence, the maximum energy absorption for WEC2 and WEC3 is achieved for  $d_{net} = 0.5r_0$ , where the  $p_j(\omega)$  peak is approximately equal to  $30 \text{ kW/m}^2$ . Moreover, for these two WECs, the frequency range, where adequate amount of power is absorbed, becomes narrower compared to the case of WEC1 and WEC4.

Regarding the power absorbed by the whole array (Figure 12c), the placement of the WECs at any of the three smallest examined net radial distances (i.e.,  $d_{net} \leq 0.5r_0$ ) does not introduce any significant differences on  $p(\omega)$ . Moreover, the aforementioned placement leads to arrays that show the best power absorption ability compared to the rest of the examined  $d_{net}$  cases, with a  $p(\omega)$  peak value approximately equal to  $120 \text{ kW/m}^2$ . Taking all the above into account and aiming at forming arrays that enable an adequate power absorption ability for both the seaward and the leeward WECs, we chose  $d_{net} = 0.25r_0$  as the most appropriate net radial distance for placing the hemispherical-shaped WECs around the monopile.

Finally, Figure 13 shows the effect of the presence of the monopile on the power absorption ability of the hemispherical-shaped WECs for the case of  $d_{net} = 0.25r_0$ . In the case of WEC1 and WEC4 (Figure 13a), the presence of the monopile in the leeward side of these WECs results in an  $\approx 33\%$  decrease of the  $p_j(\omega)$ ,  $j = 1$  and  $4$ , peak value; however, it enhances the power ability of WEC1 and WEC4 at  $1.0 \text{ rad/s} < \omega < 1.9 \text{ rad/s}$ . The shadow effects induced by the bottom-mounted cylinder reduce the power absorption ability of the WECs situated in the leeward side of the monopile (Figure 13b) at  $1.1 \text{ rad/s} < \omega < 1.9 \text{ rad/s}$ , while, moreover, they lead to an  $\approx 11\%$  decrease of the  $p_j(\omega)$ ,  $j = 1$  and  $4$ , peak value. As for the total power absorbed by the whole array (Figure 13c), it is evident that the presence of the monopile negatively affects the power absorption ability of the array, since it results in an  $\approx 20\%$  decrease of the  $p(\omega)$  peak value.

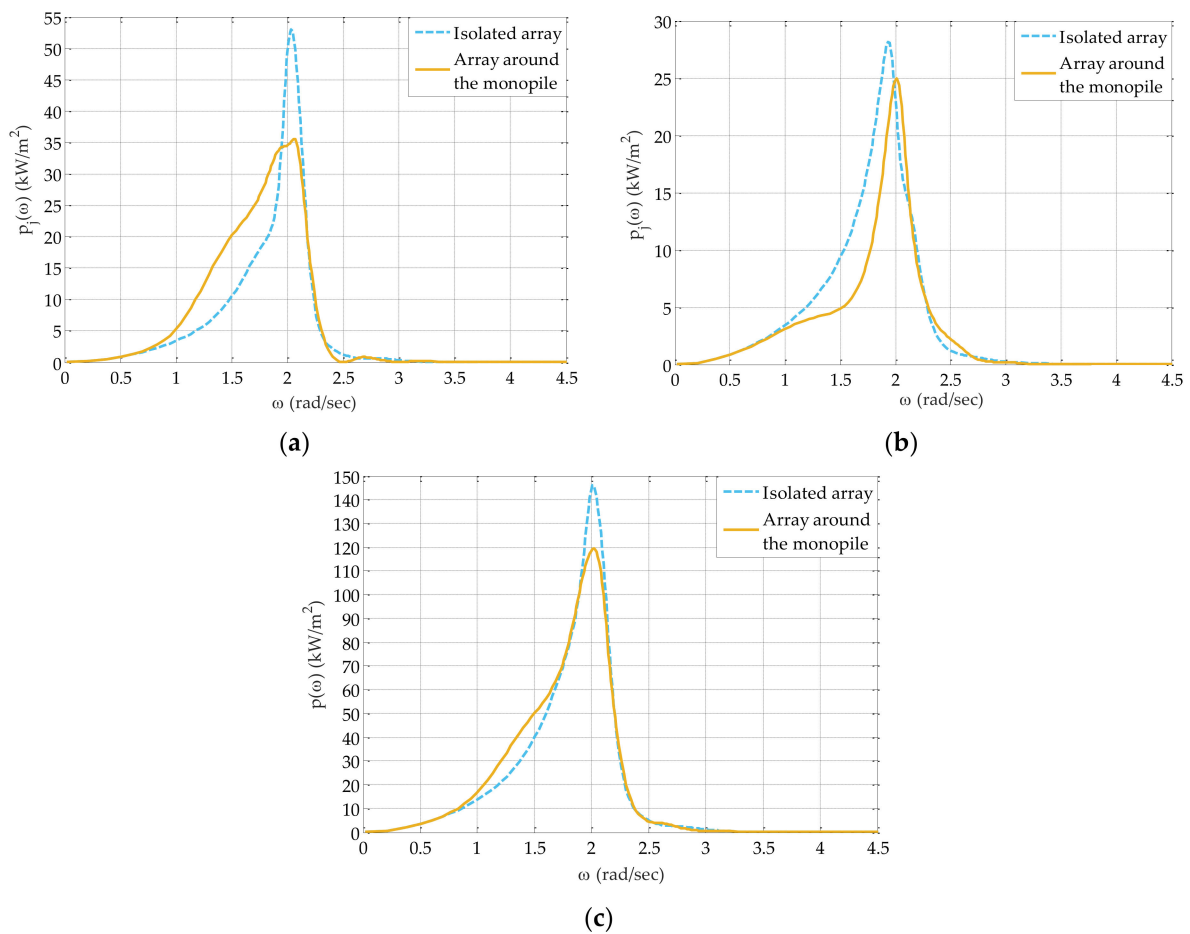


**Figure 13.** Comparison of the mean power absorbed by the hemispherical-shaped WECs with and without (isolated array) the monopile for  $\beta = 0^\circ$  and  $d_{net} = 0.25r_0$  : (a) WEC1 and WEC4; (b) WEC2 and WEC3; (c) whole array.

#### 4.3. Effect of the Incident Wave Direction on the Power Absorption Ability of the Array

In this section, we examine the effect of the incident wave direction,  $\beta$ , on the mean power absorbed by the array consisting of oblate spheroidal WECs with  $d_{net} = 0.125r_0$  and hemispherical-shaped WECs with  $d_{net} = 0.25r_0$ . It is recalled that for a given WEC geometry, the aforementioned  $d_{net}$  value corresponds to the best net radial distance for placing the WECs around the monopile in terms of power absorption ability. The corresponding results are shown in Figure 14, where the variation of  $p(\omega)$  as a function of  $\omega$  is presented for  $\beta = 0^\circ$  (head waves),  $\beta = 22.5^\circ$ , and  $45^\circ$  (oblique waves). In the case of the oblate spheroidal WECs (Figure 14a), the increase of  $\beta$  enhances the power absorption ability of the array, while the exact opposite trend is observed for the array with the hemispherical-shaped WECs (Figure 14b). Hence, for the oblate spheroidal WECs, the action of oblique waves with  $\beta = 45^\circ$  or “equivalently” the orientation of the array in a manner that enables only one of the WECs to be situated in the seaward side of the monopile leads to the best power absorption ability. On the other hand, the array consisting of hemispherical-shaped WECs perform better under the action of head incident waves (i.e.,  $\beta = 0^\circ$ ) or “equivalently” when two WECs of the array are situated in the seaward side of the monopile.

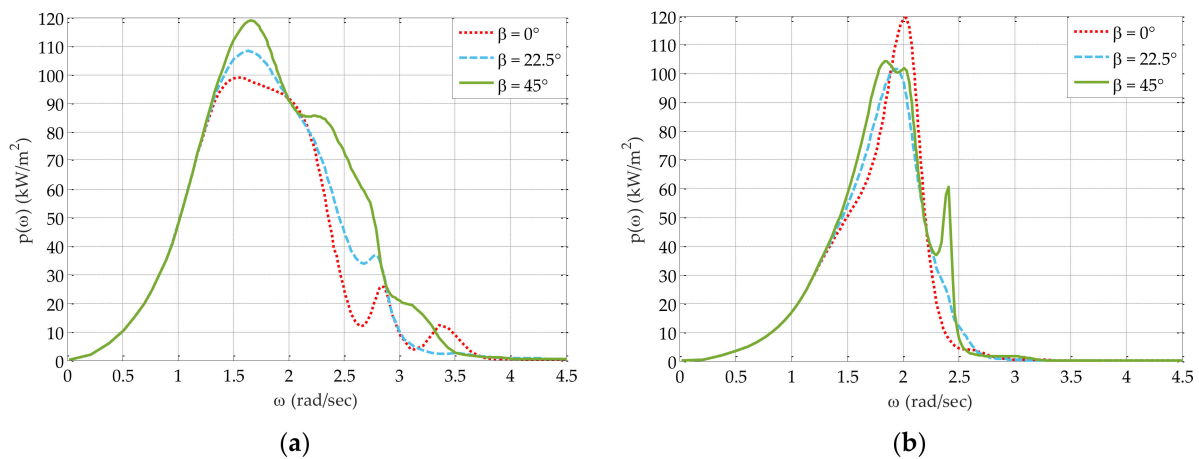


**Figure 14.** Effect of  $\beta$  on the mean power absorbed by the array with (a) oblate spheroidal WECs and  $d_{net} = 0.125r_0$ ; (b) hemispherical-shaped WECs and  $d_{net} = 0.25r_0$ .

In addition to the above and aiming at determining the array configuration (WECs' geometry and net radial distance) that shows the best power absorption ability, we compare the power absorbed by the two aforementioned arrays (oblate spheroidal WECs with  $d_{net} = 0.125r_0$  and hemispherical-shaped WECs with  $d_{net} = 0.25r_0$ ) for a given incident wave direction. The relevant comparison is made with the aid of Figure 15. Under the action of waves with  $\beta = 0^\circ$  (Figure 15a), the array consisting of oblate spheroidal WECs shows a smaller  $p(\omega)$  peak value compared to the array with the hemispherical-shaped WECs. However, by deploying oblate spheroidal WECs, the frequency range, where adequate amount of power is absorbed, becomes much wider. Indicatively, the oblate spheroidal WECs absorb power larger than  $80 \text{ kW/m}^2$  at  $1.3 \text{ rad/s} < \omega < 2.2 \text{ rad/s}$ , which is a frequency range almost three times wider compared to the corresponding one ( $1.8 \text{ rad/s} < \omega < 2.1 \text{ rad/s}$ ) observed for the hemispherical-shaped WECs. Under the action of oblique waves (Figure 15b,c), it is evident that the utilization of oblate spheroidal WECs around the monopile enhances the power absorption ability of the array, since compared to the hemispherical-shaped WECs, adequate power is absorbed at much wider frequency ranges, while, moreover, larger  $p(\omega)$  peak values are observed. From a physical point of view, this trend can be attributed to a better contribution of WEC4 and WEC3 (Figure 4) to the array's power absorption ability in the case of the oblate spheroidal WECs. More specifically, under the action of oblique waves, the hydrodynamic interactions among the hemispherical-shaped WECs and between these WECs and the monopile affect the heave exciting forces and the responses of WEC4 in a manner that significantly reduces its power absorption ability (relevant results are not cited here due to space constraints). Hence, the contribution of WEC4 to the power absorption ability of the array is smaller in the case of the hemispherical-shaped WECs compared to the oblate spheroidal ones. Furthermore, it is evident that by increasing  $\beta$ , the power absorption ability of WEC3 increases for both examined geometries, since shadow effects induced by the monopile are mainly observed for WEC2. However, as in the case of  $\beta = 0^\circ$ , for the oblate spheroidal device, the frequency range, where adequate power is absorbed, is much wider compared to the hemispherical-shaped WEC.

Taking into account all the above, the array with the oblate spheroidal WECs situated at  $d_{net} = 0.125r_0$  around the monopile could be considered as the most efficient array configuration in terms of power absorption ability among all cases examined in the present paper.

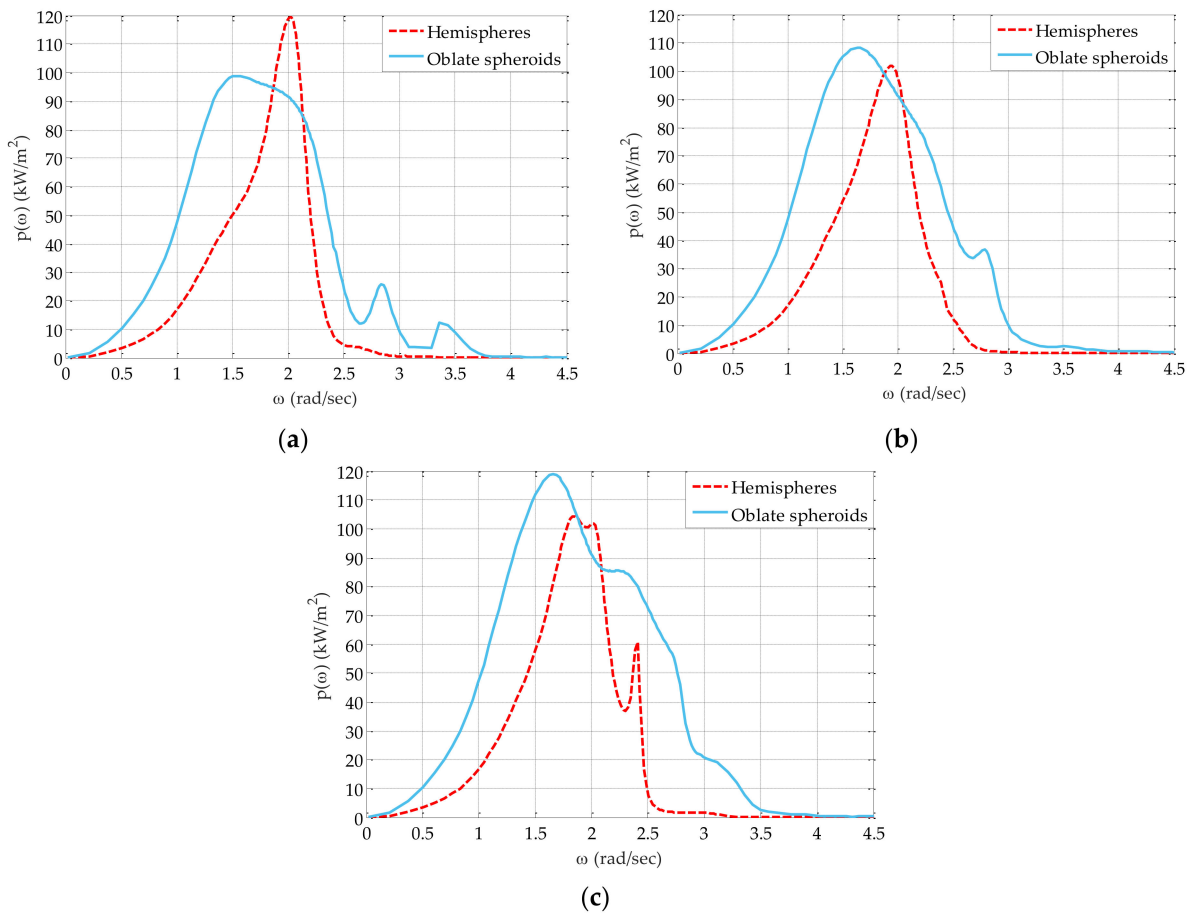


**Figure 15.** Comparison of the mean power absorbed by the array with oblate spheroidal ( $d_{net} = 0.125r_0$ ) and hemispherical-shaped ( $d_{net} = 0.25r_0$ ) WECs for (a)  $\beta = 0^\circ$ ; (b)  $\beta = 22.5^\circ$ ; (c)  $\beta = 45^\circ$ .

#### 4.4. Power Absorption Ability of the Most Efficient Array Configuration by Utilizing an “Active” PTO Mechanism

In all previous sections, the assessment of the performance of the array for different WEC geometries,  $d_{net}$  and  $\beta$  values, along with the determination of the most efficient array configuration (WECs’ geometry and net radial distance) were implemented by deploying a linear PTO mechanism of constant damping coefficient,  $b_{PTO}$ , appropriately tuned in terms of maximizing energy absorption at the natural frequency of the corresponding single, isolated WEC (i.e.,  $b_{PTO} = B_{33}^{ISO}(\omega = \omega_{n3}^{ISO})$ ). It is evident, however, that the power absorption ability of an array configuration could also be enhanced by adequately exploiting the characteristics of the PTO mechanism itself. Motivated by this, in the present section, we investigate and assess the power absorption ability of the most efficient array configuration defined in Section 4.3 (i.e., array with oblate spheroidal WECs and  $d_{net} = 0.125r_0$ ) by utilizing a PTO mechanism (hereafter called “active” PTO mechanism) of variable with frequency damping coefficient,  $b_{PTO}(\omega)$ , which enables the appropriate adjustment of its damping coefficient along the examined frequency range. It is noted that the technology of an “active” damper is widely deployed in the automotive industry, where the relevant contemporary technological advances facilitate the adjustment of the damping coefficient within fractions of a second (e.g., [37–39]).

In order to determine the  $b_{PTO}(\omega)$  values of the “active” PTO mechanism along the examined frequency range, we utilize the envelope of a family of power absorption curves obtained for the case of the isolated oblate spheroidal WEC for various constant  $b_{PTO}$  values. The corresponding results are shown in Figure 16a, where  $p(\omega)$  for the isolated WEC is plotted for nine constant  $b_{PTO}$  values equal to  $qB_{33}^{ISO}(\omega = \omega_{n3}^{ISO})$ , with  $q$  vary-

ing between 1.0 and 5.0 with a step of 0.5 (Table 3). As expected, the consideration of  $b_{PTO} = B_{33}^{ISO}(\omega = \omega_{n3}^{ISO})$  results in the maximization of  $p(\omega)$  at  $\omega = \omega_{n3}^{ISO} = 2.282$  rad/s. However, the gradual increase of the aforementioned  $b_{PTO}$  value successively enhances the power absorption ability of the isolated WEC at lower wave frequencies, since for  $b_{PTO} = qB_{33}^{ISO}(\omega = \omega_{n3}^{ISO})$  and  $q \neq 1.0$ , larger  $p(\omega)$  peaks compared to the case of  $b_{PTO} = B_{33}^{ISO}(\omega = \omega_{n3}^{ISO})$  occur at  $\omega < 2.282$  rad/s. For example, by deploying a  $b_{PTO}$  value equal to  $5B_{33}^{ISO}(\omega = \omega_{n3}^{ISO})$ , the  $p(\omega)$  peak is increased by approximately 40% and it occurs at  $\omega = 1.2$  rad/s. It is noted that the  $b_{PTO}$  values of Table 3 are within the limits of commercial dampers existing nowadays in the market (e.g., [40]), while, moreover, values larger than  $5B_{33}^{ISO}(\omega = \omega_{n3}^{ISO})$  were not taken into account, since they did not lead to any significant increase of the WEC’s power absorption ability.

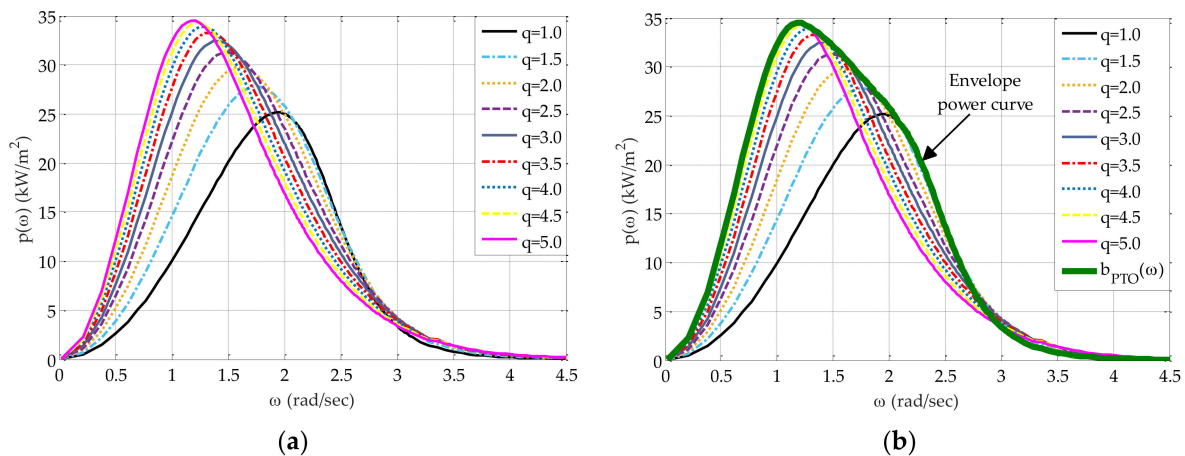


**Figure 16.** Isolated oblate spheroidal WEC: (a) power absorption curves for  $b_{PTO} = qB_{33}^{ISO}(\omega = \omega_{n3}^{ISO})$ ,  $q = 1.0, 1.5, 2.0, 2.5, 3.0, 3.5, 4.0, 4.5,$  and  $5.0$ ; (b) envelope power curve representing the utilization of an “active” PTO mechanism with  $b_{PTO}(\omega)$ .

**Table 3.** Values of  $b_{PTO} = qB_{33}^{ISO}(\omega = \omega_{n3}^{ISO})$  used for determining  $b_{PTO}(\omega)$  for the “active” PTO mechanism.

$q$	$b_{PTO}$ (kNs/m)
1.0	20.615
1.5	30.923
2.0	41.230
2.5	51.538
3.0	61.845
3.5	72.153
4.0	82.460
4.5	92.768
5.0	103.075

Having obtained the family of the nine power curves, we determined their envelope (green curve in Figure 16b). This envelope curve represents the power absorbed by the isolated oblate spheroidal WEC in the case of an “active” PTO mechanism, where the variable with frequency  $b_{PTO}$  (i.e.,  $b_{PTO}(\omega)$ ) is appropriately tuned in terms of maximizing energy absorption at a given incident wave frequency or at a given frequency range. The advantage of this “active” PTO mechanism is twofold. Firstly, it gives the potential to absorb adequate amount of power at a very wide frequency range. For example, by utilizing the “active” PTO mechanism, the power absorption ability of the oblate spheroidal WEC becomes larger than  $25 \text{ kW/m}^2$  at  $0.75 \text{ rad/s} < \omega < 2.1 \text{ rad/s}$ , contrary to any of the nine cases, where a constant  $b_{PTO}$  was considered. Secondly, it leads to the occurrence of the  $p(\omega)$  peak at lower wave frequencies, facilitating the efficient employment of this WEC

and, thus, of the proposed hybrid offshore wind and wave energy exploitation system at marine areas characterized by low-frequency sea waves.

Having determined the  $b_{PTO}(\omega)$  values of the “active” PTO mechanism along the examined frequency range, we applied this mechanism for the most efficient array configuration consisting of oblate spheroidal WECs situated at  $d_{net} = 0.125r_0$  around the monopile in order to assess the array’s power absorption ability under both regular and irregular waves of incident wave direction  $\beta = 45^\circ$ . For regular waves, the corresponding results are shown in Figure 17, where the power absorbed by the whole array in the case of the “active” PTO mechanism (i.e., utilization of  $b_{PTO}(\omega)$ ) is compared with the power absorbed for a PTO mechanism of constant  $b_{PTO}$  equal to  $B_{33}^{ISO}(\omega = \omega_{n3}^{ISO})$ . It is evident that the utilization of the “active” PTO mechanism leads to a significant improvement of the power absorption ability of the array, since it leads to an  $\approx 50\%$  increase of the  $p(\omega)$  peak and facilitates adequate power absorption at low wave frequencies.

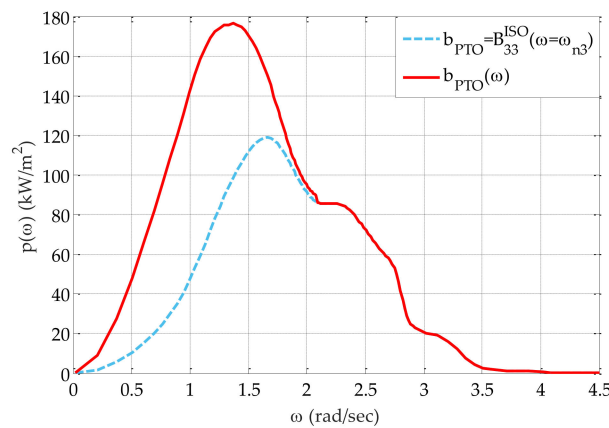


**Figure 17.** Comparison of the mean power absorbed by the array with oblate spheroidal WECs and  $d_{net} = 0.125r_0$  under the action of regular waves with  $\beta = 45^\circ$  by utilizing (a) a PTO with constant  $b_{PTO}$  equal to  $B_{33}^{ISO}(\omega = \omega_{n3}^{ISO})$ ; (b) an “active” PTO with  $b_{PTO}(\omega)$ .

Under the action of irregular waves, for a given sea state described by a spectrum with significant wave height,  $H_s$ , and peak period,  $T_p$ , we obtain the power absorbed by the array,  $p(H_s, T_p)$ , using the following equation:

$$p(H_s, T_p) = \sum_{j=1}^4 p_j(H_s, T_p) \tag{14}$$

where  $p_j(H_s, T_p), j = 1, \dots, 4$ , is the power absorbed by the  $j^{\text{th}}$  WEC, calculated as follows:

$$p_j(H_s, T_p) = \int_0^\infty S_{JONSWAP}(\omega|H_s, T_p) p_j(\omega) d\omega \tag{15}$$

In Equation (14),  $S_{JONSWAP}(\omega|H_s, T_p)$  is the spectral density of the JONSWAP spectrum, which is deployed in the present paper for describing the incident waves, while the symbol “|” is used to denote given values of  $H_s$  and  $T_p$ . The spectral density  $S_{JONSWAP}(\omega|H_s, T_p)$  is obtained by applying the following equation [41]:

$$S_{JONSWAP}(\omega|H_s, T_p) = [1 - 0.287 \ln(\gamma)] \frac{5}{16} H_s^2 \omega_p^4 \omega^{-5} \exp\left(-\frac{5}{4} \left(\frac{\omega}{\omega_p}\right)^{-4}\right) \gamma^{\exp(-0.5(\frac{\omega - \omega_p}{\sigma \omega_p})^2)} \tag{16}$$

where  $\omega_p = 2\pi/T_p$ ,  $\gamma$  is the non-dimensional peak shape parameter equal to 3.3 and  $\sigma$  is the spectral width parameter equal to 0.07 for  $\omega \leq \omega_p$  and 0.09 for  $\omega > \omega_p$ . It is noted that in Equation (15),  $p_j(\omega)$  for each frequency component of the spectrum is calculated using Equation (13), which corresponds to incident waves of unit amplitude.

The power absorption ability of the most efficient array configuration is assessed for 225 sea states (i.e.,  $H_s$  and  $T_p$  combinations), with  $H_s$  varying between 0.5 m and 7.5 m with a step of 0.5 m and  $T_p$  between 3.0 s and 17 s with a step equal to 1.0 s. The corresponding results are shown in Figure 18, where the contours of  $p$  for the aforementioned sea states are plotted for the array with and without the utilization of the “active” PTO mechanism. In the latter case (Figure 18a), the maximum value of  $p$  corresponds to 340 kW ( $H_s = 7.5$  m and  $T_p = 4.0$  s), while by utilizing the “active” PTO mechanism (Figure 18b), the maximum power absorbed by the array becomes equal to 535 kW ( $H_s = 7.5$  m and  $T_p = 4.0$  s), representing an  $\approx 60\%$  increase. One more important aspect to note is that the power iso-contours for the array with the “active” PTO mechanism are much wider along the  $T_p$ -axis compared to the array, where the PTO mechanism has a constant  $b_{PTO}$  value. This in turn illustrates that the array with the “active” PTO mechanism shows a better power absorption ability for a larger number of sea states. Even for small  $H_s$  values, the power absorption ability of the array is still maintained at adequate levels along the examined  $T_p$  range.

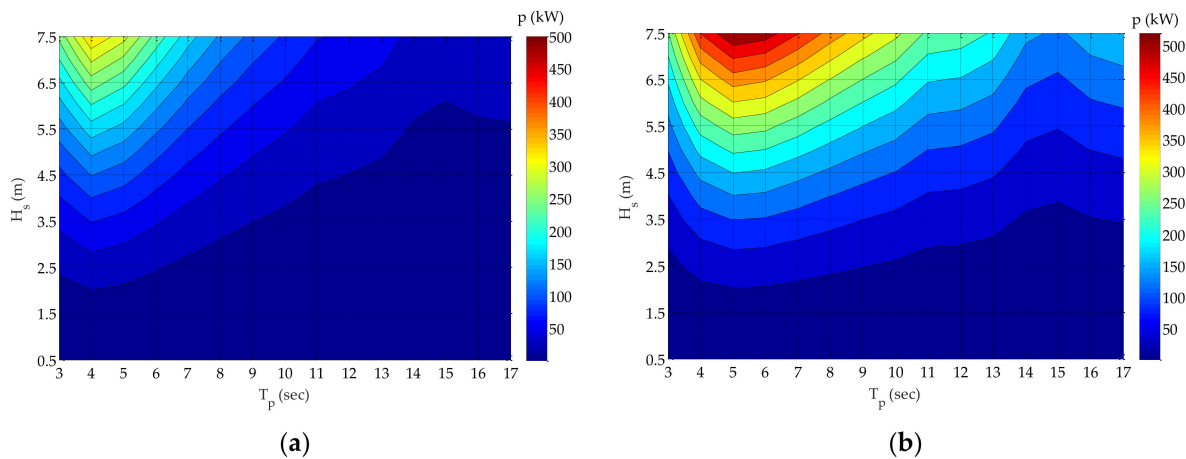


**Figure 18.** Comparison of power absorbed by the array the oblate spheroidal WECs and  $d_{net} = 0.125r_0$  under the action of irregular wave with  $\beta = 45^\circ$  by utilizing (a) a PTO with constant  $b_{PTO}$  equal to  $B_{33}^{ISO} (\omega = \omega_{n3}^{ISO})$ ; (b) an “active” PTO with  $b_{PTO}(\omega)$ .

### 5. Conclusions

In this paper, a frequency-based numerical analysis was implemented to investigate the performance (hydrodynamic behavior and power absorption) of a circular array of four semi-immersed heaving WECs distributed uniformly around a hybrid wind–wave monopile support structure. Arrays consisting of oblate spheroidal and hemispherical-shaped WECs were examined and compared, while focus was given to the effect of characteristic design parameters (WECs’ net radial distance from the monopile, incident wave direction, and PTO characteristics) on the power absorption ability of the array. The main conclusions of the present investigation for the specific WECs’ geometrical characteristics and water depth conditions considered can be summarized as follows:

- With regard to the effect of the net radial distance from the monopile on the array’s power absorption ability, this effect depends strongly upon the examined frequency range for the array consisting of oblate spheroidal WECs. Specifically, at low wave frequencies, the aforementioned array shows the best power absorption ability by placing the WECs at the smallest examined net radial distance ( $d_{net} = 0.125r_0$ ), while at higher wave frequencies, the exact opposite trend is observed, namely, the best power absorption ability occurs for the array placed at the largest examined net radial distance ( $d_{net} = 1.5r_0$ ). This trend advocates the potential efficient utilization of the oblate spheroidal WECs at marine areas characterized by either low-frequency or

high-frequency sea waves. It is noted, however, that for  $d_{net} = 0.125r_0$ , the frequency range where adequate amount of power is absorbed becomes quite wide. This feature combined with constructability issues as well as with the fact that most real sea states are characterized by low-frequency sea waves leads to the selection of  $d_{net} = 0.125r_0$  as the most appropriate net radial distance for placing the array around the monopile. On the other hand, the array consisting of hemispherical-shaped WECs shows the best power absorption ability when the WECs are situated at small net radial distances from the monopile (i.e., for  $d_{net} = 0.125r_0$ ,  $0.25r_0$ , and  $0.5r_0$ ). The value of  $d_{net} = 0.25r_0$  is considered the most appropriate net radial distance for placing the array, since it facilitates adequate power absorption ability for both the seaward and the leeward WECs.

- The power absorption ability of the array with oblate spheroidal WECs and  $d_{net} = 0.125r_0$  is greatly improved under the action of oblique waves with  $\beta = 45^\circ$ , while the opposite trend is observed for the array with hemispherical-shaped WECs and  $d_{net} = 0.25r_0$ , where the best power absorption ability occurs for head waves (i.e.,  $\beta = 0^\circ$ ).
- The deployment of oblate spheroidal WECs around the monopile enhances the power absorption ability of the array, since compared to the hemispherical-shaped WECs, adequate power is absorbed at much wider frequency ranges, while, moreover, larger power peak values may be observed depending upon the incident wave direction. Hence, the array with the oblate spheroidal WECs situated at  $d_{net} = 0.125r_0$  around the monopile presents the most efficient array configuration (WECs' geometry and net radial distance) in terms of power absorption ability.
- The utilization of an "active" PTO mechanism, facilitating the consideration of a variable with frequency PTO damping coefficient,  $b_{PTO}(\omega)$ , that maximizes energy absorption at a given incident wave frequency or at a given frequency range, significantly enhances the power absorption ability of the array compared to the deployment of a PTO mechanism with a constant  $b_{PTO}$ . For the most efficient array configuration (i.e., oblate spheroidal WECs with  $d_{net} = 0.125r_0$ ), the deployment of this "active" PTO mechanism under the action of oblique regular waves results in an  $\approx 50\%$  increase of the power peak, as well as to a wider frequency range, extending mainly towards lower frequencies, where adequate power absorption is achieved. Positive conclusions are also derived in the case of irregular waves, since by utilizing the "active" PTO mechanism, an  $\approx 60\%$  increase of the maximum power absorbed by the array occurs while, moreover, the array configuration shows a better power absorption ability for a larger number of sea states.

The present investigation can be extended by appropriately coupling the hydrodynamic model with an optimization algorithm, aiming at defining the optimum in terms of power absorption maximization and array configuration (WECs' geometry and net radial distance) while utilizing an "active" PTO mechanism. Recalling that the WECs along with the monopile present components of a bottom-mounted hybrid offshore wind and wave energy exploitation system, it would also be interesting to analyze in time domain the performance of the whole system and assess the effect of the existence of the WECs on the structural integrity of the monopile.

**Author Contributions:** Conceptualization, E.L., S.G., and P.C.; methodology, S.G., P.C., and E.L.; software, S.G. and P.C.; formal analysis, S.G. and P.C.; investigation, S.G., P.C., and E.L.; writing—original draft preparation, S.G. and P.C.; writing—review and editing, E.L.; supervision, E.L. All authors have read and agreed to the published version of the manuscript.

**Funding:** This research received no external funding.

**Data Availability Statement:** The data presented in this study are available on request from the corresponding author.

**Conflicts of Interest:** The authors declare no conflict of interest.

## References

1. Bahaj, A.S. Generating electricity from the ocean. *Renew. Sustain. Energy Rev.* **2011**, *15*, 3399–3416. [CrossRef]
2. Iglesias, G.; Carballo, R. Wave energy potential along the Death Coast (Spain). *Energy* **2009**, *34*, 1963–1975. [CrossRef]
3. Oceans of Energy—European Ocean Energy Roadmap 2010–2050. Available online: [https://www.icoe-conference.com/publication/oceans\\_of\\_energy\\_european\\_ocean\\_energy\\_roadmap\\_2010\\_2050/](https://www.icoe-conference.com/publication/oceans_of_energy_european_ocean_energy_roadmap_2010_2050/) (accessed on 2 November 2020).
4. Perez-Collazo, C.; Astariz, S.; Abanades, J.; Greaves, D.; Iglesias, G. Co-located Wave and Offshore Wind Farms: A Preliminary Case Study of a Hybrid Array. In Proceedings of the 34th International Conference in Coastal Engineering, Seoul, Korea, 16–20 June 2014; Lynett, P., Ed.; Curran Associates Inc.: New York, NY, USA, 2016; p. 34. [CrossRef]
5. Astariz, S.; Perez-Collazo, C.; Abanades, J.; Iglesias, G. Towards the optimal design of a co-located wind-wave farm. *Energy* **2015**, *84*, 15–25. [CrossRef]
6. Astariz, S.; Iglesias, G. Enhancing wave energy competitiveness through co-located wind and wave energy farms. A review on the shadow effect. *Energies* **2015**, *8*, 7344–7366. [CrossRef]
7. Pérez-Collazo, C.; Jakobsen, M.M.; Buckland, H.; Fernández-Chozas, J. Synergies for a Wave-Wind Energy Concept. In Proceedings of the European Offshore Wind Energy Conference, Frankfurt, Germany, 19–21 November 2013; The European Wind Energy Association: Brussels, Belgium, 2013.
8. Jeffrey, H.; Sedgwick, J. ORECCA European Offshore Renewable Energy Roadmap. Available online: [http://orecca.rse-web.it/doc\\_info/ORECCA\\_EU\\_offshore\\_Renewable\\_Energy\\_Roadmap.pdf](http://orecca.rse-web.it/doc_info/ORECCA_EU_offshore_Renewable_Energy_Roadmap.pdf) (accessed on 2 November 2020).
9. Karimirad, M. *Offshore Energy Structures*; Springer International Publishing: Cham, Switzerland, 2014.
10. Colin, W. (Ed.) Offshore Wind in Europe—Key Trends and Statistics 2019. 2020. Available online: <https://windeurope.org/wp-content/uploads/files/about-wind/statistics/WindEurope-Annual-Offshore-Statistics-2019.pdf> (accessed on 2 November 2020).
11. Lynch, K.; Murphy, J. *Overview of Offshore Wind and Ocean Energy Technologies*; Public Report of Marine Renewable Integrated Application (MARINA) Platform Project: Cork, Ireland, 2012.
12. Michailides, C.; Gao, Z.; Moan, T. Experimental and numerical study of the response of the offshore combined wind/wave energy concept SFC in extreme environmental conditions. *Mar. Struct.* **2016**, *50*, 35–54. [CrossRef]
13. Michailides, C.; Gao, Z.; Moan, T. Experimental study of the functionality of a semisubmersible wind turbine combined with flap-type wave energy converters. *Renew. Energy* **2016**, *93*, 675–690. [CrossRef]
14. Michailides, C.; Luan, C.; Gao, Z.; Moan, T. Effect of Flap Type Wave Energy Converters on the Response of a Semi-Submersible Wind Turbine in Operational Conditions. In Proceedings of the 33rd International Conference on Ocean, Offshore and Arctic Engineering, San Francisco, CA, USA, 8–16 June 2014; p. OMAE2014-24065. [CrossRef]
15. Muliawan, M.J.; Karimirad, M.; Moan, T. Dynamic response and power performance of a combined Spar-type floating wind turbine and coaxial floating wave energy converter. *Renew. Energy* **2013**, *50*, 47–57. [CrossRef]
16. Muliawan, M.J.; Karimirad, M.; Gao, Z.; Moan, T. Extreme responses of a combined spar-type floating wind turbine and floating wave energy converter (STC) system with survival modes. *Ocean Eng.* **2013**, *65*, 71–82. [CrossRef]
17. Gao, Z.; Moan, T.; Wan, L.; Michailides, C. Comparative numerical and experimental study of two combined wind and wave energy concepts. *J. Ocean Eng. Sci.* **2016**, *1*, 36–51. [CrossRef]
18. Wang, Y.; Zhang, L.; Michailides, C.; Wan, L.; Shi, W. Hydrodynamic response of a combined wind-wave marine energy structure. *J. Mar. Sci. Eng.* **2020**, *8*, 253. [CrossRef]
19. Bachynski, E.E.; Moan, T. Point Absorber Design for a Combined Wind and Wave Energy Converter on a Tension-Leg Support Structure. In Proceedings of the 32nd International Conference on Ocean, Offshore and Arctic Engineering, Nantes, France, 9–14 June 2013; p. OMAE2013-10429. [CrossRef]
20. Karimirad, M.; Koushan, K. WindWEC: Combining Wind and Wave Energy Inspired by Hywind and Wavestar. In Proceedings of the 2016 IEEE International Conference on Renewable Energy Research and Application, Birmingham, UK, 20–23 November 2016; pp. 96–101. [CrossRef]
21. Karimirad, M.; Michailides, C. Effects of Structural Design Parameters on the Hydrodynamic Interaction and Response of the Combined WindWEC Concept. In Proceedings of the 12th European Wave and Tidal Energy Conference, Cork, Ireland, 27 August–1 September 2017.
22. Karimirad, M.; Michailides, C. Effects of Misaligned Wave and Wind Action on the Response of the Combined Concept WindWEC. In Proceedings of the 37th International Conference on Ocean, Offshore and Arctic Engineering, Madrid, Spain, 17–22 June 2018; p. OMAE2018-77078. [CrossRef]
23. Mazarakos, T.; Konispoliatis, D.; Katsaounis, G.; Polyzos, S.; Manolas, D.; Voutsinas, S.; Soukissian, T.; Mavrakos, S.A. Numerical and experimental studies of a multi—purpose floating TLP structure for combined wind and wave energy exploitation. *J. Mediterr. Mar. Sci.* **2019**, *20*, 745–763. [CrossRef]
24. Lee, H.; Poguluri, S.K.; Bae, Y.H. Performance analysis of multiple wave energy converters placed on a floating platform in the frequency domain. *Energies* **2018**, *11*, 406. [CrossRef]
25. Perez-Collazo, C.; Greaves, D.; Iglesias, G. A novel hybrid wind-wave energy converter for jacket-frame substructures. *Energies* **2018**, *11*, 637. [CrossRef]
26. Perez-Collazo, C.; Pemberton, R.; Greaves, D.; Iglesias, G. Monopile-mounted wave energy converter for a hybrid wind-wave system. *Energy Convers. Manag.* **2019**, *199*, 111971. [CrossRef]

27. Ren, N.; Ma, Z.; Fan, T.; Zhai, G.; Ou, J. Experimental and numerical study of hydrodynamic responses of a new combined monopile wind turbine and a heave type wave energy converter under typical operational conditions. *Ocean Eng.* **2018**, *159*, 1–8. [[CrossRef](#)]
28. Power Technology. Available online: <https://www.power-technology.com/projects/greenoceanenergywav/> (accessed on 2 November 2020).
29. Wave Star. Available online: <http://wavestarenergy.com/> (accessed on 2 November 2020).
30. Miquel, A.M.; Antonini, A.; Archetti, R.; Bozzi, S.; Lamberti, A. Non-linear modelling of a heaving point absorber: The surge effect. *Int. J. Mar. Energy* **2017**, *19*, 95–109. [[CrossRef](#)]
31. Bozzi, S.; Miquel, A.M.; Scarpa, F.; Antonini, A.; Archetti, R.; Passoni, G.; Gruosso, G. Wave energy production in Italian offshore: Preliminary design of a point absorber with tubular linear generator. In Proceedings of the 4th International Conference on Clean Electrical Power: Renewable Energy Resources Impact, Alghero, Italy, 11–13 June 2013; pp. 203–208. [[CrossRef](#)]
32. Gaeta, M.G.; Segurini, G.; Moreno, A.M.; Archetti, R. Implementation and validation of a potential model for a moored floating cylinder under waves. *J. Mar. Sci. Eng.* **2020**, *8*, 131. [[CrossRef](#)]
33. WAMIT Theory Manual. Available online: <https://www.wamit.com/Publications/tmanual.pdf> (accessed on 2 November 2020).
34. Lee, C.H.; Newman, J.N. Computation of wave effects using the panel method. In *Numerical Models in Fluid-Structure Interaction*; Chakrabarti, S., Ed.; WIT Press: Southampton, UK, 2005; pp. 211–251.
35. Falnes, J.; Kurniawan, A. *Ocean Waves and Oscillating Systems: Linear Interactions Including Wave-Energy Extraction*, 2nd ed.; Cambridge University Press: Cambridge, UK, 2020; pp. 20–23.
36. Beels, C.; Henriques, J.C.C.; De Rouck, J.; Pontes, M.T.; De Backer, G.; Verhaeghe, H. Wave Energy Resource in the North Sea. In Proceedings of the 7th European Wave and Tidal Energy Conference, Porto, Portugal, 11–13 September 2007.
37. Acura, Active Damper System. Available online: <https://www.acura.com/mdx/modals/active-damper-system#:~:text=The%20Active%20Damper%20System%20can,road%20requires%20high%2Dperformance%20handling> (accessed on 2 November 2020).
38. KONI, KONI ACTIVE Technology. Available online: [https://www.koni.com/en-US/Cars/Technology/ACTIVE\\_Technology/](https://www.koni.com/en-US/Cars/Technology/ACTIVE_Technology/) (accessed on 2 November 2020).
39. General Kinetics. Active Shock Brand Semi Active Dampers. Available online: <http://www.generalkinetics.com/products/military/active-shock-semi-active-dampers.php> (accessed on 2 November 2020).
40. ENDINE. Available online: <https://www.itt-infrastructure.com/en-US/Home> (accessed on 2 November 2020).
41. Det Norske Veritas–Germanischer Lloyds (DNV–GL). *Environmental Conditions and Environmental Loads, Recommended Practice DNVGL-RP-C205*; DNV-GL: Oslo, Norway, 2017.